A WRF-Chem study of the greenhouse gas column and in situ surface concentrations observed at Xianghe, China. Part 1: Methane (CH$_4$)

Sieglinde Callewaert[1,4], Minqiang Zhou[1,2], Bavo Langerock[1], Pucai Wang[3], Ting Wang[3], Emmanuel Mahieu[4], and Martine De Mazière[1]

[1]Royal Belgian Institute for Spacy Aeronomy (BIRA-IASB), Brussels, Belgium
[2]State Key Laboratory of Atmospheric Environment and Extreme Meteorology, Institute of Atmospheric Physics, Chinese Academy of Sciences, Beijing, China
[3]CNRC & LAGEO, Institute of Atmospheric Physics, Chinese Academy of Sciences, Beijing, China
[4]UR SPHERES, Department of Astrophysics, Geophysics and Oceanography, University of Liège, Liège, Belgium

Correspondence: Sieglinde Callewaert (sieglinde.callewaert@aeronomie.be), Minqiang Zhou (minqiang.zhou@aeronomie.be)

Abstract. This study is the first of two companion papers which investigate the temporal variability of CO$_2$, CH$_4$ and additionally CO concentrations measured at the Xianghe observation site near Beijing in China using the Weather Research and Forecast model coupled with Chemistry (WRF-Chem), aiming to understand the contributions from different emission sectors and the influence of meteorological processes. Simulations of the in situ (PICARRO) and remote sensing (TCCON-affiliated) measurements are produced by the model's greenhouse gas option, called WRF-GHG, from September 2018 until September 2019. The present study discusses the results for CH$_4$. The model shows good performance, after correcting for biases in boundary conditions, achieving correlation coefficients up to 0.66 for near-surface concentrations and 0.65 for column-averaged data. The simulations use separate tracers for different source sectors and revealed that energy, residential heating, waste management and agriculture are the primary contributors to the CH$_4$ concentrations, with the energy sector having a greater impact on column measurements than surface concentrations. Monthly variability is linked to both emission patterns and meteorological influences, with advection of either clean or polluted air masses from the North China Plain playing a significant role. The diurnal variation of the in situ concentrations due to planetary boundary layer dynamics is quite well captured by WRF-GHG. Despite capturing the key variability of the CH$_4$ observations, the model displays a seasonal bias, likely originating from an incorrect seasonality in the emissions from agricultural and/or waste management activities. Our findings highlight the value of WRF-GHG to interpret both surface and column observations at Xianghe, offering source sector attribution and insights in the link with local and large-scale winds based on the simultaneously computed meteorological fields. However, they also highlight the need to improve the knowledge on the seasonal CH$_4$ cycle in northern China to obtain more accurate emission data and boundary conditions for high-resolution modeling.

1 Introduction

Carbon dioxide (CO_2) and methane (CH_4) are the most important anthropogenic greenhouse gases (GHG), contributing to climate change. Driven by human activities, the atmospheric burden of both species has been increasing over the last 200 years to unprecedented levels (Masson-Delmotte et al., 2021). Moreover, CH_4 has a 28 times larger global warming potential than CO_2 over a period of 100 year and a 10 times shorter atmospheric lifetime. Controlling CH_4 emissions is therefore a priority to mitigate climate change in the near future (Saunois et al., 2020).

Because of rapid industrialization in the past decades and its heavy dependence on coal, China is the world's largest emitter of CO_2 and CH_4 (Friedlingstein et al., 2022; Worden et al., 2022). The main anthropogenic CO_2 sources in China are industry, power generation, residential and commercial activities and transportation (Zhao et al., 2012), while sectors such as coal mining, livestock, rice paddies, landfills and wastewater management are the largest contributors to the CH_4 emissions in China (Chen et al., 2022). China has pledged to reach its carbon peak by 2030 and neutrality by 2060. To help battle climate change and reach these goals, it is essential to have accurate observations of the GHG concentrations. Not only does atmospheric monitoring aid in revealing sources and sinks and controlling the impact of mitigation measures, but by studying temporal variations a better understanding of the carbon cycle and its interactions with the atmosphere can be achieved.

Since 2018, both ground-based in situ and remote sensing observations of GHGs have been deployed at the Xianghe observatory, which is located about 50 km southwest of Beijing. Its location in the center of the Beijing-Tianjin-Hebei (BTH) megalopolis makes it an interesting site to study the properties and variability of GHGs in a polluted area. The remote sensing observations are made by a Fourier Transform Infrared (FTIR) spectrometer and are part of the international Total Column Carbon Observing Network (TCCON), while the in situ concentrations are measured by a PICARRO cavity ring-down spectroscopy (CRDS) analyzer that samples air from a tower at an altitude of 60 m above the ground.

Our work aims to perform a comprehensive analysis of both in situ and column observations of CO_2, CH_4 and additionally CO at Xianghe to gain a better understanding of the causes of the observed temporal variabilities and complement previous studies. The present article is the first of two companion papers where the focus of the current work lies on the CH_4 observations. A second paper (in preparation) will cover the analysis for CO_2 and CO.

Some first insights in the observed CH_4 time series at Xianghe were made by Yang et al. (2020) and Ji et al. (2020). They found that the seasonal cycle of XCH_4 is different compared to those at other TCCON sites at similar latitude, with larger concentrations in summer and autumn and lower values in spring. Furthermore, the column observations of CO_2, CH_4 and CO show a large day-to-day variability and are correlated with each other. Yang et al. (2020) showed that the high values are related to both local pollution and pollution originating from the south, while low concentrations are corresponding with clean airmasses from more remote regions in the north.

To achieve our goal, we will simulate the time series at a high spatial resolution with the WRF-Chem model for greenhouse gases (WRF-GHG). This widely used regional atmospheric transport model simulates the 3-D concentrations together with meteorological fields without chemical interactions, which is generally a valid assumption regarding the regional domain and the relatively long atmospheric lifetimes of the target species ($\sim$ 100 yrs for CO_2, $\sim$ 10 yrs for CH_4 and several weeks for

CO)(Dekker et al., 2017). Nevertheless, both CH_4 and CO are prone to chemical reactions in the atmosphere, making this assumption a simplification of actual conditions, which should be taken into account when analyzing the results. WRF-GHG has already shown to be a useful tool to study CO_2 fluxes and variability in China (Dayalu et al., 2018; Liu et al., 2018; Li et al., 2020; Dong et al., 2021). However, and to our best knowledge, applications to CH_4 or CO observations in China have not been reported yet. Elsewhere, this model was successfully used to analyze comparable observations (Zhao et al., 2019; Hu et al., 2020; Park et al., 2020; Callewaert et al., 2022). Therefore, this study will additionally assess the model's capability of simulating these time series in north China and highlight its strengths and weaknesses in this region.

This work is structured as follows: in Sect. 2 the Xianghe site and its observations are described, together with the XCH_4 product of TROPOMI (the TROPOspheric Monitoring Instrument onboard Sentinel-5P), which will give additional insight into the results. Further, an overview of the WRF-GHG model system is given and the approach used to compare the model simulations with the different measurements. Section 3 presents the results and discussion: the main model performance is evaluated in Sect.3.1, followed by an analysis of the contributions from different source sectors to the CH_4 observations at Xianghe in Sect.3.2. Section 3.3 explores potential causes of the observed seasonal bias in the model simulations, while Sect. 3.4 examines the key meteorological processes influencing CH_4 variability. Further, a comparison with TROPOMI XCH_4 is conducted in Sect. 3.5 to investigate the potential overestimation of emissions from a coal mine source near Tangshan. Finally, Sect.4 summarizes the key findings and conclusions for CH_4.

2   Data, models and methods

2.1   Xianghe site

The observation site is situated in Xianghe county (39.7536° N, 116.96155° E; 30 m a.s.l.), a suburban area in the Beijing-Tianjin-Hebei (BTH) region in north China. The center of Xianghe is about 2 km to the east of the site, while the metropolitan cities of Beijing and Tianjin are located about 50 km to the northwest and 70 km to the south-southeast, respectively (see Fig. 1b). Cropland and irrigated cropland are the predominant kind of vegetation in the area. The East Asian Monsoon, which causes hot, humid summers with plenty of precipitation and cold, dry winters, determines the climate.

Since 1974, atmospheric observations are made at the Xianghe observatory by the Institute of Atmospheric Physics (IAP), Chinese Academy of Sciences (CAS). In June 2016 a FTIR spectroscopy instrument (Bruker IFS 125HR) was installed on the roof of the observatory, two years later, a solar tracker was added to the setup and continuous measurements are made from June 2018 onwards. This ground-based remote sensing instrument measures spectra in the infrared and is affiliated with TCCON (Wunch et al., 2011; Zhou et al., 2022), providing total column-averaged dry air mole fractions (denoted as Xgas) of CO_2, CH_4 and CO. In the current study, the GGG2020 data version (Laughner et al., 2024) is used. Depending on the weather and measurement status, observations occur every 5-20 min. TCCON measurements are performed under clear sky conditions only. The measurement uncertainty is about 6 ppb for XCH_4. Further details about the instrument and retrieval methodology can be found in Yang et al. (2020).

Additionally, in situ mole fractions of CO_2 and CH_4 are measured by a PICARRO cavity ring-down spectroscopy G2301
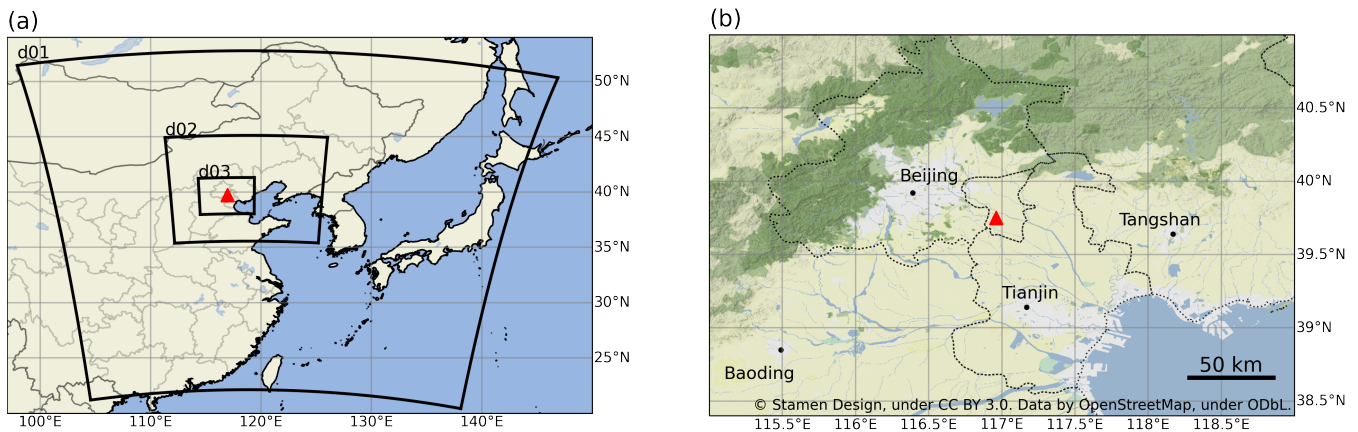
Figure 1. (a) Location of the WRF-GHG domains, with horizontal resolutions of 27 km (d01), 9 km (d02) and 3 km (d03). All domains have 60 (hybrid) vertical levels extending from the surface up to 50 hPa. (b) Terrain map including the largest cities in the region of Xianghe, roughly corresponding to d03. The location of the Xianghe site is indicated by the red triangle in both maps.

analyzer since June 2018. The instrument samples air from an inlet fixed at 60 m above the ground on a tower. More detail about the measurement setup is given in Yang et al. (2021). The measurement uncertainty is 1 ppb for CH_4.

2.2 TROPOMI

The TROPOMI instrument on board the Sentinel-5 Precursor (S5P) satellite is observing the Earth on a polar sun-synchronous
90 orbit. With a daily global coverage, it measures solar backscatter in the near and shortwave infrared absorption bands of which column-average mixing ratios of CH_4 can be retrieved. In the current study, the bias-corrected reprocessed L2 RemoTec-S5P XCH_4 product from SRON (ESA, 2021) was used, where a quality filter of 0.5 was applied. This L2 product was evaluated at Xianghe by Yang et al. (2020) and Tian et al. (2022): they found a small negative bias of -0.6% and -0.39% with TCCON XCH_4, respectively. These values are well within the mission requirements of 1.5 % and therefore indicate a good quality of
95 TROPOMI XCH_4 in this part of China.

2.3 WRF-GHG modeling system

We use the Weather Research and Forecasting model coupled with Chemistry version 4.1.5 (WRF-Chem, Grell et al. (2005); Skamarock et al. (2019); Fast et al. (2006)) in its greenhouse gas option, called WRF-GHG (Beck et al., 2011). WRF-GHG is an Eulerian atmospheric transport model that simulates the 3-D concentration of trace gases at every time step simultaneously with
100 meteorological fields, neglecting chemical reactions. The model configuration consists of three nested domains with increasing resolution in a Lambert Conformal projection (see Fig. 1a). The parent domain (d01) has 134 by 130 grid cells of 27×27 km^2 and covers a large part of China, Mongolia, North and South Korea and Japan. The second domain (d02), which has 133 by 121 grid cells of 9×9 km^2, mainly covers north China. Finally, the innermost domain (d03) has a resolution of 3×3 km^2 over

Table 1. Overview of physical parameterization options used for WRF-GHG simulations.

Physics	Scheme name	Option
Microphysics	Morrison 2-moment	10
Longwave radiation	RRTMG	4
Shortwave radiation	RRTMG	4
Planetary boundary layer	Mellor-Yamada-Janjic	2
Surface layer	Eta similarity	2
Cumulus (only in d01)	Grell 3D Ensemble	5
Land surface	Unified Noah Land Surface Model	2

145 by 124 grid cells and almost completely covers BTH. There are 60 vertical levels between the surface and 50 hPa. A set of physical parameterization schemes was chosen (see Table 1) after performing several sensitivity tests which are detailed in Appendix A. Remark that the cumulus parameterization scheme was only applied in the outermost domain (d01). Given the wide range of global anthropogenic emission datasets available and the significance of these fluxes to simulate accurate concentrations in regions with large anthropogenic activity such as BTH, several anthropogenic emission inventories were also included in these sensitivity tests.

2.3.1 Input data and parameterization

The model was driven by the hourly European Centre for Medium-Range Weather Forecasts (ECMWF) global ERA5 reanalysis data set ($0.25° \times 0.25°$, Hersbach et al. (2023a, b)) for meteorological fields. The concentration fields for CO_2 and CH_4 are initialized by the 3-hourly Copernicus Atmosphere Monitoring Service (CAMS) global reanalysis for greenhouse gases (EGG4), while the 6-hourly reactive gases product is used for CO (EAC4, Inness et al. (2019)). These CAMS reanalysis data sets are also used at the model domain boundaries to represent influences coming from outside the parent domain (d01). They are remapped with mass conservation to the WRF-GHG domains using the CDO software (Climate Data Operators, Schulzweida (2020)). The evolution of these initial and lateral boundary conditions inside the domain over time is stored in a separate tracer, the so-called background tracer. Similarly, the evolution of concentrations caused by emissions within the boundaries of d01 is saved in different tracers, dependent on their source sector. The sum of all tracers, including the background, gives the total simulated concentrations which can be compared to the observations.

The simulations are re-initialized with the ECMWF ERA5 data every 30 h, starting at 18:00 UTC the previous day with a 6 h spin-up period, as done in other WRF-GHG modeling studies (Feng et al., 2016; Park et al., 2018; Pillai et al., 2011). Every day at 00:00 UTC, the tracer fields from the previous run are copied to the new simulation to ensure continuous transport of the concentrations.

We conducted sensitivity tests to identify a set of physical parameterization schemes and anthropogenic fluxes that provide appropriate simulations for all three species (CH_4, CO_2, and CO) across the different observation methods (in situ and remote sensing). The details of these tests are provided in Appendix A. Our findings indicate that the anthropogenic fluxes from CAMS-

Table 2. Overview of mapping between the five broad sectors used in this study (first column) and the emission sectors provided by CAMS-GLOB-ANT v5.3 (second column) and REAS v3.2.1 (third column).

This study	CAMS-GLOB-ANT (for CO_2 and CH_4)	REAS (for CO)
Energy	Power generation (ene)	Power plants point
	Fugitives (fef)	Power plants non-point
	Oil refineries and transformation sector (ref)	
Industry	Industrial processes (ind)	Industry
Transport	Road transportation (tro)	Road transport
	Off Road transportation (tnr)	Other transport
	Ships (shp)	
Residential & Waste	Residential, commercial and other combustion (res)	Domestic
	Solid waste and waste water (swd)	
Agriculture	Agriculture soils (ags)	
	Agricultural waste burning (awb)	
	Agriculture livestock (agl)	

GLOB-ANT v5.3 (Granier et al., 2019; Soulie et al., 2023) for CO_2 and CH_4, and from REAS v3.2.1 (Regional Emission Inventory in Asia, Kurokawa and Ohara (2020)) for CO offer the best alignment with the Xianghe observations. We released all fluxes in the lowest model layer near the surface and multiplied them with temporal factors of CAMS-TEMPO (Guevara et al., 2021) to account for hourly and daily variation. Remark that both chosen anthropogenic inventories additionally provide sector-specific information. To include this information in our simulations, different sectors are linked to separate tracers. The 11 sectors from CAMS-GLOB-ANT were aggregated into five broad sectors to make the model simulations computationally less expensive. A similar aggregation was performed on the REAS sectors. The mapping is given in Table 2. This will allow us to track the respective contributions to the total simulated concentrations of the following source categories: energy, industry, transportation, residential & waste and agriculture. More detail about what is included in every sub-sector can be found in the documentation of the respective data set.

Further, biomass burning emissions are coming from the Fire INventory from NCAR (FINN v2.5, Wiedinmyer et al. (2011)) for all species. The observation-based global pCO_2 climatology from Landschützer et al. (2017) is used to represent the ocean-atmosphere exchange of CO_2, while the CH_4 fuxes from wetlands are taken from the WetCHARTS v1.0 climatology (Bloom et al., 2017). Finally, WRF-GHG calculates the biogenic CO_2 fluxes online based on the Vegetation Photosynthesis and Respiration Model (VPRM, Mahadevan et al. (2008); Ahmadov et al. (2007)). It uses its own calculated 2 m temperature and downward shortwave radiation together with surface reflectance data from the Moderate Resolution Imaging Spectroradiameter (MODIS) onboard the Aqua and Terra satellites. The extra required parameters for VPRM are taken from Li et al. (2020).

2.4 Comparing observations with WRF-GHG simulations

2.4.1 Xianghe in situ observations

The WRF-GHG model cell which covers the location of the instrument is selected to compare with the in situ observations. Because the concentrations are measured at an altitude of 60 m.a.g.l., this WRF-GHG profile is interpolated to that altitude, using the model surface as ground level. Finally, the observations are averaged over a period of 30 minutes around the hourly model output.

2.4.2 Xianghe TCCON remote sensing observations

The same model cell as for the in situ observations is used to compare with the column observations. The five TCCON observations that are closest in time with the WRF-GHG output, but deviate no more than 15 minutes, are averaged and used for the comparison. The model profile is extended above 50 hPa with the TCCON a priori profile and then smoothed by using the averaging kernels in order to account for the instrument and retrieval characteristics (Rodgers and Connor, 2003). Note that an alternative approach would be to extend the model profiles with the CAMS reanalysis that is used as initial and lateral boundary conditions. However, the accuracy issues with CAMS CH_4 data in the stratosphere are well-documented (Ramonet et al., 2021; Agustí-Panareda et al., 2023), and would introduce known biases into our study. Moreover the optimized a priori profiles of the TCCON GGG2020 data show improved accuracy in the stratosphere (Laughner et al., 2023), supporting our decision to utilize this data for extending the model profiles.

2.4.3 TROPOMI observations

To compare the spatial XCH_4 distribution of TROPOMI with those of WRF-GHG, the model profiles are extended above 50 hPa with the TROPOMI a priori column number density profiles of CH_4 and dry air (mol m^{-2}) to ensure that both products in the comparison cover the same altitude range. Since a typical CH_4 profile shows a sharp decrease in the upper layers of the atmosphere, this part has a non-negligible impact on the column-averaged mole fraction. Further, the extended WRF-GHG CH_4 profiles are smoothed with the TROPOMI column averaging kernels and a priori profiles following Apituley et al. (2023). The column number density profiles of CH_4 and dry air are calculated from the hourly 3-D WRF-GHG output as follows:

$$\rho_i^{CH_4} = \nu_i^{CH_4} \rho_i^{da}, \text{ with } \rho_i^{da} = \frac{P_i}{RT_i} \frac{1}{1+1.6075q_i} \tau_i. \tag{1}$$

In the above equation $\nu_i^{CH_4}$ is the CH_4 dry air volume mixing ratio (ppb) and ρ_i^{da} the dry air column number density in WRF-GHG layer i. The dry air column number density ρ_i^{da} is calculated according to the ideal gas law, where P_i, T_i and q_i are the air pressure (Pa), temperature (K) and water vapor mixing ratio with respect to dry air (kg kg^{-1}), respectively. The thickness of layer i (m) is represented by τ_i. Finally, R is the ideal gas constant 8.3145 J K^{-1} mol^{-1}. Note that 1.6075 is the ratio of the molar mass of dry air with respect to the molar mass of water to convert wet air to dry air.

TROPOMI has an equator crossing time of around 13:30 local solar time, so we compute the equivalent simulated XCH_4 by taking the average over 12h-15h LT. Note that we use the model simulations from the d02 domain (which has a horizontal

resolution of 9×9 km^2) for this analysis, instead of d03 as for the comparisons with Xianghe observations, since a larger spatial extent is advantageous for a statistically effective comparison with TROPOMI.

Using the HARP toolset (part of the Atmospheric Toolbox, https://atmospherictoolbox.org/) for TROPOMI and the CDO software (Schulzweida, 2020) for WRF-GHG, both XCH$_4$ products are then binned to a common spatial grid to enable a
180 quantitative analysis: we have chosen a regular latitude-longitude grid with a horizontal resolution of 0.05°.

3 Results and discussion

3.1 Overall model performance

With the model settings as elaborated in Sect. 2.3, WRF-GHG was run from 15 August 2018 to 1 September 2019. However, the first two weeks were regarded as a spin-up phase, so the analysis is made on one full year of data: from 1 September 2018
185 until 1 September 2019. This conservative spin-up period is implemented to ensure thorough mixing of the tracers within the domain. The complete data set can be accessed on https://doi.org/10.18758/P34WJEW2 (Callewaert, 2023).

Due to the absence of qualitative meteorological observations at the Xianghe site, the simulated near-surface temperature and 10-m wind fields within domain d03 were evaluated against the publicly available Global Hourly - Integrated Surface Database (ISD) from the National Centers for Environmental Information (NCEI) to assess model performance for key meteorological
190 parameters. Considering the reported precision of the observational data, the analysis reveals that the WRF-GHG model adequately captures the primary surface meteorological conditions within the study domain and period. We therefore assume that significant systematic errors in the simulated transport are unlikely.

An overview of the simulated and observed time series of the CH$_4$ concentrations at Xianghe is shown in Fig. 2, together with the model error. To further illustrate the distribution of the differences between model and observations, a histogram is given
195 in Fig. 3. For the column observations, the model shows a mean underestimation of -3.03 ppb, with a moderate correlation of 0.56 (Table 3). At the surface level, the data were divided into afternoon (13:00–18:00 LT) and nighttime (03:00–08:00 LT) periods for statistical analysis, as models generally perform better in simulating concentrations during the afternoon when the lower atmosphere is better mixed. The definition of these time periods is based on the daily maximum and minimum values, as will be discussed later in Sect. 3.4.2. Indeed, the correlation is higher during the afternoon (0.66) compared to nighttime (0.42),
200 with mean bias errors of 14.22 ppb and 12.68 ppb, respectively (see Table 3). Additionally, significantly larger errors were found at night, indicating greater challenges for the model in accurately capturing nighttime values compared to afternoon.

The moderate correlation coefficients are likely due to a seasonality in the bias: WRF-GHG is underestimating the CH$_4$ data at Xianghe in summer and autumn (June - November) and slightly overestimating them in winter (January - March), which is especially visible for the column data in Fig. 2c.

205

Possible sources of this bias are inaccuracies in the background values, misrepresentation of CH$_4$ sources and sinks within WRF-GHG, or a combination of these factors. Given CH$_4$'s long atmospheric lifetime, background values significantly contribute to the total simulated signal, as also illustrated by the mean values for the background and total simulated tracer in
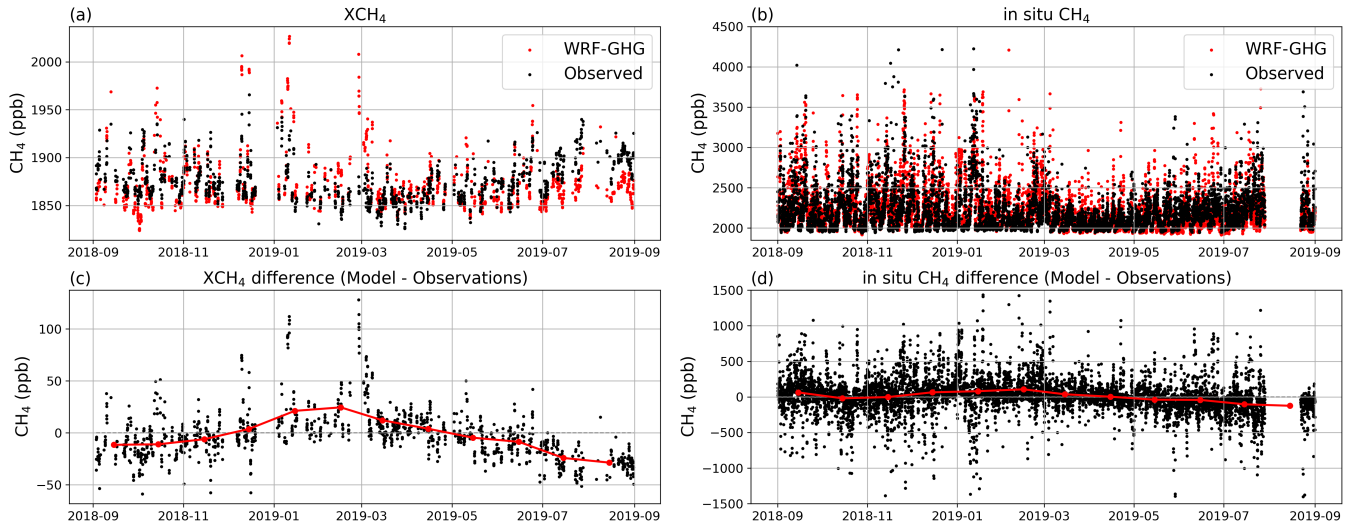
Figure 2. Time series of the observed (black) and simulated (red) (a) XCH$_4$ and (b) insitu CH$_4$ concentrations at the Xianghe site. Panels (c) and (d) show the differences between WRF-GHG simulations and observations for XCH$_4$ and in situ CH$_4$, respectively. Data points are hourly. The red points in (c) and (d) represent the monthly mean differences.

Table 3. Statistics of the model-data comparison of the ground-based CH$_4$ observations at the Xianghe site from 1 September 2018 until 1 September 2019. We present the mean bias error (BIAS), root mean square error (RMSE) and Pearson correlation coefficient (CORR). The mean bias error and root mean square error are given in ppb. For in situ observations, the data is split in afternoon (13-18 LT) and night (3-8 LT) hours.

	insitu CH$_4$ (afternoon)	insitu CH$_4$ (night)	XCH$_4$
BIAS	14.22	12.68	-3.03
RMSE	159.74	334.06	23.96
CORR	0.66	0.42	0.56

the top of Table 4. We therefore start by further examining the global CAMS reanalysis which is used to represent the inflow and outflow at the model domain boundaries. In the CAMS validation report by Ramonet et al. (2021), a similar seasonal bias between CAMS CH$_4$ and TCCON is found. To explore this pattern in more detail and include Xianghe in the analysis, we reproduce their calculations for several TCCON sites at similar latitudes (Karlsruhe (49.1° N), Orleans (48.0° N), Garmisch (47.5° N), Park Falls (45.9° N), Rikubetsu (43.5° N), Lamont (36.6° N), Tsukuba (36.0° N), Edwards (35.0° N), Pasadena (34.1° N), Saga (33.2° N), and Hefei (31.9° N)) for the period of interest, as shown in Fig. 4. Indeed, we find a seasonal bias where CAMS is overestimating TCCON XCH$_4$ from December until May and showing a small underestimation in the rest of the period. The bias at Xianghe ranges from 13.17 ppb in February 2019 to -6.56 ppb in August 2019 (monthly mean differences). The monthly mean bias of WRF on the other hand, ranges between 24.49 ppb in February 2019 and -28.70 ppb in August 2019 and shows a significantly larger amplitude than the CAMS bias. Moreover, the same seasonal pattern is found in
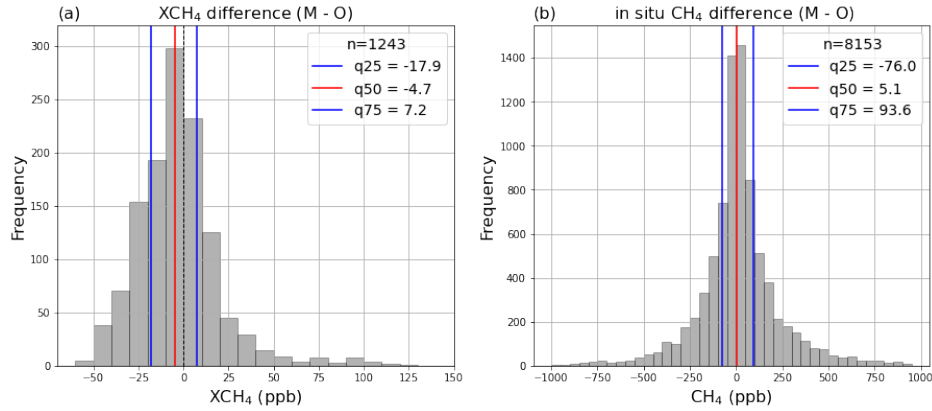
Figure 3. Distribution of difference between model and observations for (a) XCH_4 and (b) in situ CH_4 (ppm), using hourly data points. The red line indicates the median difference, while the blue lines are the first and third quartiles.

Table 4. Statistics of the total simulated CH_4 concentrations and the different tracer contributions over the complete simulation period. Q1 and Q3 represent the first and third quartile, respectively, between which 50 % of the data fall.

	XCH_4 (ppb)				in situ CH_4 (ppb)			
	Q1	median	mean	Q3	Q1	median	mean	Q3
Total	1900.74	1916.18	1927.36	1942.42	2028.75	2132.50	2212.50	2302.58
Background	1885.79	1890.75	1891.34	1896.57	1912.83	1927.69	1925.37	1938.20
Biomass burning	0.00	0.00	0.00	0.00	0.00	0.00	0.00	0.00
Energy	2.61	11.13	19.04	28.90	12.03	49.67	105.88	135.21
Residential (& waste)	2.65	5.86	8.17	10.72	31.24	65.49	94.33	122.11
Industry	0.07	0.17	0.21	0.30	0.77	1.63	2.29	2.99
Transportation	0.06	0.12	0.15	0.20	0.66	1.40	2.00	2.58
Agriculture	2.00	4.75	7.56	9.49	24.95	51.77	76.08	97.30
Wetlands	0.02	0.12	0.56	0.62	0.09	0.66	4.17	3.91
Termites	0.17	0.29	0.34	0.46	1.13	2.02	2.37	3.17
Total tracers	9.86	24.76	36.02	51.21	102.75	209.15	287.13	377.48

the time series of the differences for the in situ data (Fig. 2d). Ramonet et al. (2021) assume the seasonal bias within CAMS is related to an inaccurate representation of the seasonal cycle of surface emissions and/or the OH sink. Similarly, the remaining WRF-GHG bias likely arises from errors in the seasonality of the CH_4 emissions and/or neglecting the reaction of CH_4 with OH. This will be further investigated in Sect. 3.3.

In the rest of this work, we have applied a bias correction to the WRF-GHG simulations by subtracting the monthly mean difference between CAMS and TCCON XCH_4, averaged over all sites (except Pasadena due to outlier behavior) between 30
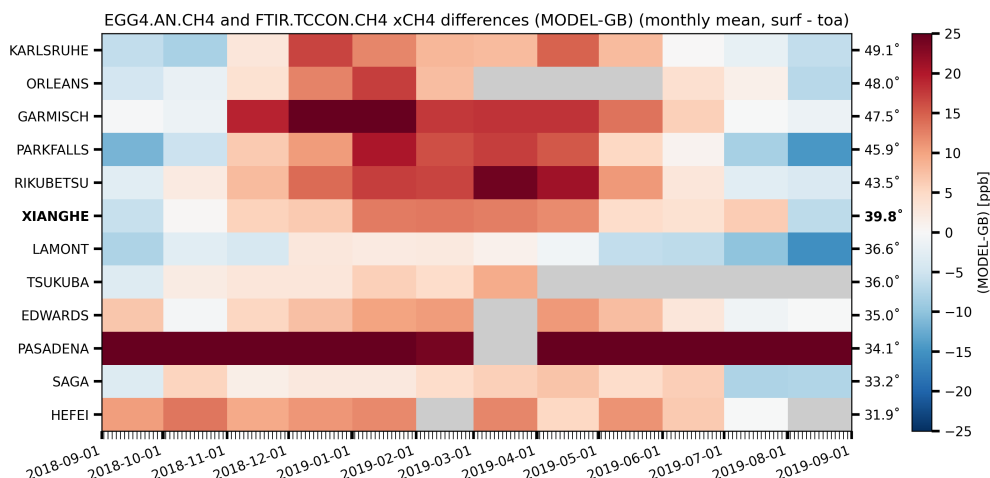
Figure 4. Monthly mean difference (in ppb) between CAMS reanalysis model and TCCON XCH$_4$ between 30 - 50° N over the simulation period of this study.

- 50° N, from the background tracer. The updated statistical metrics are given in Table 5. The correlation coefficient for the column data slightly improves to 0.67, where for the surface concentrations the bias correction has only a negligible impact on the model-data comparison. The remaining monthly mean bias for XCH$_4$ (in situ CH$_4$) ranges between 13.04 ppb (95.20 ppb) in February 2019 and -25.70 ppb (-121.25 ppb) in August 2019, which is still larger than the measurement uncertainty of 6 ppb (1 ppb).

Table 5. Same as Table 3 but with bias corrected model values.

	insitu CH$_4$ (afternoon)	insitu CH$_4$ (night)	XCH$_4$
BIAS	8.43	6.88	-8.10
RMSE	158.29	333.22	22.35
CORR	0.66	0.43	0.67

3.2 Sector contributions to observed concentrations

All fluxes that are included in WRF-GHG are tracked in separate tracers, as explained in Sect. 2.3. This allows us to disentangle the total simulated concentrations into the different tracer contributions and evaluate the influence of different source sectors on the observations at Xianghe, as well as their respective importance. An overview of the monthly mean values is shown in Fig. 5, while additionally the median and interquartile range of the complete period are given in Table 4. Note that all simulated hours were used for this analysis, not just the ones coinciding with observations.
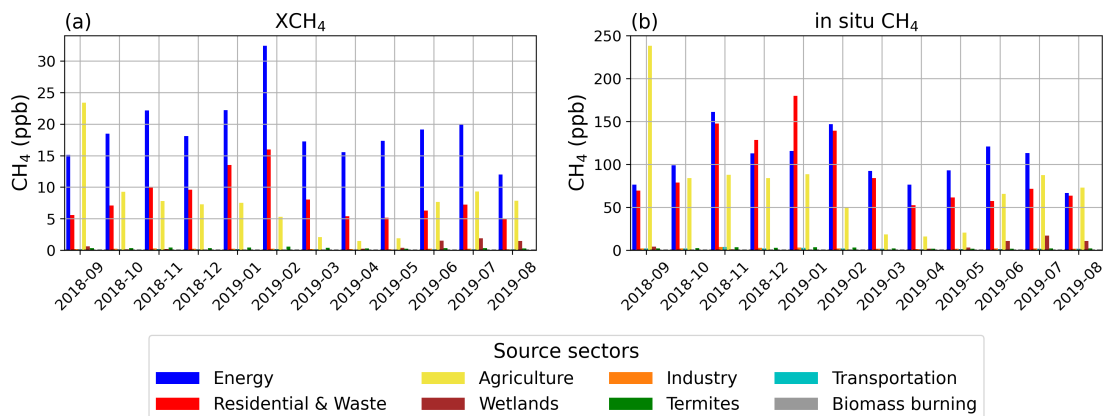
Figure 5. Monthly mean tracer contributions above the background for (a) XCH$_4$ and (b) in situ CH$_4$ simulated concentrations at Xianghe.

For CH$_4$, the simulated signal at Xianghe is mainly determined by three sectors: energy, residential & waste (which combines both residential heating and waste management sectors) and agriculture. They respectively contribute with a median enhancement of 11.13 ppb, 5.86 ppb and 4.75 ppb above the background for the columns and 49.67 ppb, 65.49 ppb and 51.77 ppb near the surface (see Table 4). Furthermore there is a small contribution from wetlands in summer, peaking in July with a median tracer contribution of 1.49 ppb for the columns and 10.65 ppb near the surface. Other sectors such as industry, transportation, termites and biomass burning seem to be irrelevant at Xianghe. Overall, the total tracer enhancement is about ten times larger for the in situ concentrations compared to the column-averaged values.

The fact that the dominant source sectors (agriculture, residential heating, waste management and energy (which is mainly coal mining in this case)) are not known for releasing CH$_4$ at elevated altitudes, supports our choice to implement the emissions only in the lowest model layer.

Futhermore, remark that for the in situ concentrations, the three dominant sectors are roughly equally important, while for the column concentrations we find a larger impact of the energy sources: the relative mean enhancement of the energy tracer is 52.87% for the column concentrations, while it is only 36.88% for the surface concentrations. When looking at the mean vertical profiles of the different tracer contributions above Xianghe (Fig. 6a) we see that the contributions from the energy sector are generally found at a higher altitude compared to other sectors. High concentrations near the surface are associated with emission sources nearby, while those aloft are likely caused by long-distance pollutant transport in the free troposphere. Therefore, we assume that this difference between column and surface energy contribution is because the strongest energy sources are situated in Shanxi (the largest coal producing province in China), which is much further away from Xianghe than for example the strongest residential (mainly Beijing and Tianjin) and agricultural sources, see Fig. 6b-d.

In Fig. 5, we further observe a larger residential signal in winter, where the median tracer contribution peaks with 13.43 ppb in February for the columns and with 132.75 ppb in January, near the surface. Meanwhile, the influence from agriculture reaches its maximum in September (monthly median values of 14.46 ppb for XCH$_4$ and 196.07 ppb for in situ CH$_4$) and its minimum
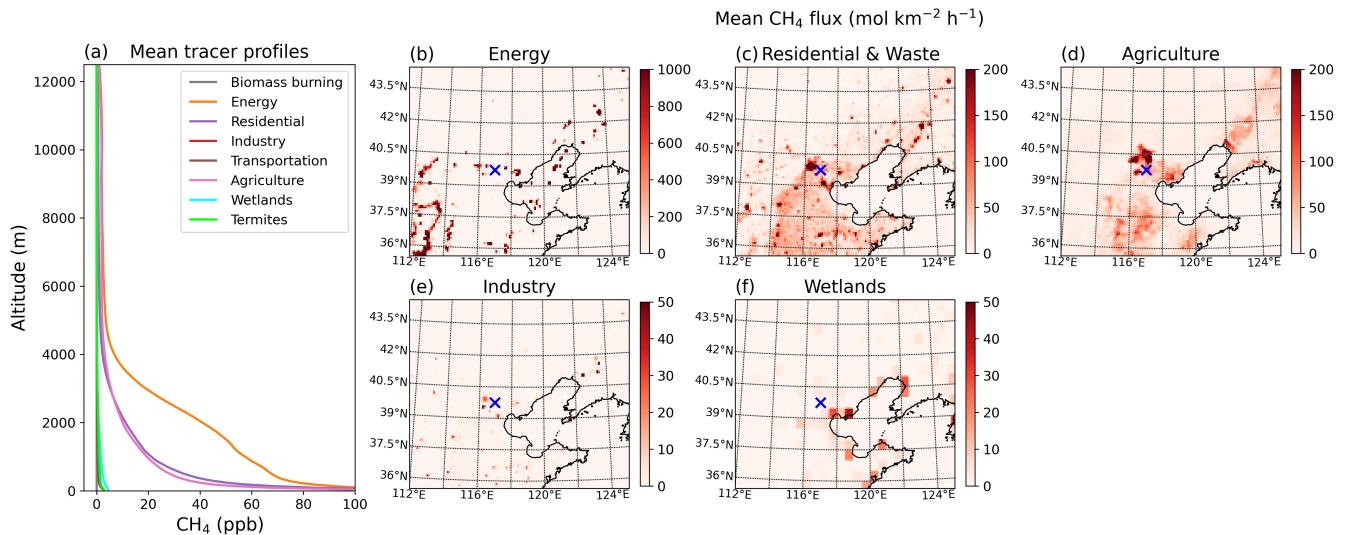
Figure 6. (a) Mean vertical profile of the tracer fields in WRF-GHG for CH$_4$ at Xianghe. All simulated hours were used for this plot. (b-f) Maps of the mean CH$_4$ flux (mol km^{-2} h^{-1}) in WRF-GHG domain d02 during the entire simulation period for the most important sectors. Remark that different sectors have different ranges in the colorbar. The location of the Xianghe site is indicated by the blue cross.

in March-April (monthly median values of 0.89 ppb for XCH$_4$ and 11.49 ppb for in situ CH$_4$). This corresponds with the seasonal pattern of emissions within CAMS-GLOB-ANT.

3.3 Seasonal CH$_4$ bias

In Sect. 3.1, we identified a seasonal bias in the CH$_4$ simulations (WRF-GHG underestimates CH$_4$ in summer and autumn, overestimates in winter) that could not be fully explained by a similar bias in the background data, indicating a potential bias in the seasonality of the emission data and/or a consequence of ignoring the OH sink. In this section, we first investigate the primary emission sectors that may have contributed to this seasonal bias. One of the major sources of CH$_4$ at Xianghe is the energy sector (see Sect. 3.2), primarily through emissions from the extraction, processing, storage and transport of coal, oil and natural gas. These emissions are not expected to exhibit significant monthly variation. Indeed, the energy emissions in the CAMS-GLOB-ANT inventory are relatively stable throughout the year: they show a coefficient of variation (CV, calculated as the ratio of the standard deviation to the mean) of only 0.42% for the monthly averaged values across the model domain. As a result, our focus will be on the following emission categories: agriculture, residential & waste, and wetlands.

– Agriculture. As presented in Table 2, the agricultural sector is comprised of three subsectors: soils (this is mainly rice cultivation), agricultural waste burning, and livestock (manure management and enteric fermentation). In China, rice cultivation plays a vital role but is predominantly concentrated in regions south of 35°N. In CAMS-GLOB-ANT, the most important agriculture subsector in the region of the Xianghe site is livestock. According to the emission inventory, livestock emissions in the wide region around Xianghe peak in September and reach their lowest levels in March and

April. Unfortunately, the source of these monthly variations in CH_4 emissions within the inventory is unclear, as the accompanying data set of temporal factors, CAMS-GLOB-TEMPO (Guevara et al., 2021), references constant factors for CH_4 emissions from agricultural sources. Previous research by Maasakkers et al. (2016) suggests that emissions from manure management often correlate with air temperature, with higher emissions during warmer months (May to September in this case) and lower emissions during colder months (December to February). If the true seasonality of agricultural emissions around Xianghe is indeed temperature-driven, it implies that the current inventory underestimates emissions during spring and summer (May to August) and overestimates them in winter, as it shows a peak only in September and a minimum in spring (March-April) rather than in winter. This discrepancy in the seasonality of emissions could explain the seasonal bias observed in our CH_4 simulations, pointing to inaccuracies in the representation of agricultural emissions. This is further evidenced by the contrasting model biases observed in September between near-surface and column-averaged CH_4 (Fig. 2c-d). Incorrect temporal variation of agricultural emissions implies an overestimation of the emission in September, where the current peak values are. Considering that in situ observations are more sensitive to local sources compared to column measurements, which represent a larger spatial average, and given the presence of a localized high-emission area immediately north of Xianghe (Fig. 6d), this overestimation in September would more likely lead to an overestimation of in situ CH_4 than XCH_4.

– Residential & waste. This sector represents emissions from residential, commercial and other combustion sources together with CH_4 emissions from solid waste and waste water treatment. In CAMS-GLOB-ANT, the waste sector is the most important one in the Xianghe region and assumed to be relatively constant throughout the year: monthly total CH_4 emissions between 38-41 °N and 115-119 °E range between 0.0408 Tg and 0.0452 Tg. In summer, total residential combustion emissions in the region can be as low as 0.0039 Tg per month, while in winter, they are almost of the same size as the waste emissions: 0.0357 Tg. So the seasonality of the residential & waste sector is coming from the residential part, peaking in winter. However, Hu et al. (2023) showed that CH_4 emissions from waste treatment often follow the seasonality of air temperature. Even though this study is based on observations in the Hangzhou megacity, their results could possibly be representative for the BTH region as well. This would mean that the waste emissions are underestimated in summer and/or overestimated in winter, which would match the current model-observation mismatch for CH_4.

– Wetlands. Within the WRF-GHG simulations, wetlands only show minor contributions to the surface and column data, and only in summer. Emissions are taken from the WetCHARTs v1.0 ensemble data set. In the BTH area, the main wetland areas are located close to the Bohai Sea (see Fig. 6f). However, according to WetCHARTs, these emissions are relatively small compared to those from wetlands more in the south of China. In an evaluation of the WetCHARTs ensemble against GOSAT observations by Parker et al. (2020), a general underestimation of the seasonal amplitude in China was found. Furthermore, Chen et al. (2022) showed increased posterior wetlands emissions compared to the a priori values when inferring yearly CH_4 emissions over China using TROPOMI satellite observations. This could point to an underestimation of the wetland emissions in the current study, and therefore an underestimation of CH_4 in summer.

The observed seasonal error pattern between the WRF-GHG CH_4 simulations and the Xianghe observations may be due to one or more of the reasons previously mentioned. To gain a spatial perspective on this seasonal bias, we compared the WRF-GHG XCH_4 field with TROPOMI observations. Note that this comparison with TROPOMI should be interpreted with caution, as WRF-GHG does not account for atmospheric chemistry and is assumed to not show systematic transport errors. The primary aim here is to identify suggestive spatial patterns of potential emission inaccuracies. Figure 7 shows the seasonal mean XCH_4 from both WRF-GHG and TROPOMI, as well as their normalized difference over the broader Xianghe region. To highlight seasonal variations, we subtracted the mean difference between WRF-GHG and TROPOMI over the entire simulation period (also shown in Fig. 13d) from the seasonal means, resulting in a 'normalized difference.' Overall, we find a mean bias error between WRF-GHG and TROPOMI of -10.55 ppb (or -0.56% [(TROPOMI - WRF-GHG)/WRF-GHG]), consistent with previous studies (Yang et al., 2020; Tian et al., 2022; Sha et al., 2021).

The analysis reveals a model underestimation in summer (JJA) and an overestimation in winter (DJF), see Fig. 7. The biases are smaller in spring and autumn. However, we cannot identify a distinct spatial pattern throughout the seasons that could point to errors within a specific source sector. Figure 7 shows differences on a large spatial scale, suggesting that for example the underestimation by WRF-GHG is linked to emission sources that are widespread in the region. Since the North China Plain is a livestock-dominated region with strong urbanization and industrial activities, this implies that the fluxes of either agriculture (livestock), waste treatment, or both, rather than the fluxes from wetlands, are underestimated in summer in CAMS-GLOB-ANT. Given the lack of a clear outcome from our analysis, it is likely a combination of factors.

Finally, we used backward simulations with the FLEXible PARTicle dispersion model (FLEXPART) v10.4 (Pisso et al., 2019) to evaluate the impact of the OH sink on CH_4 concentrations at Xianghe. CH_4 particles were released near the surface at the Xianghe site using the FLEXPART backward mode with and without OH reaction, at different times throughout the day and year. More specific details of the model configuration and simulations are provided in Appendix B. By comparing simulations that include or exclude the chemical reaction with OH, we estimated its influence. The results indicate a more pronounced difference in summer than in winter, with mean relative backward sensitivity differences of about 0.04%, 0.005%, 0.05%, and 0.2% in October 2018, January 2019, April 2019, and July 2019, respectively, over the entire footprint. Considering the size of CH_4 emissions within the WRF-GHG domain (Table 4), the contribution of the ignored OH reaction to the CH_4 mole fraction is around 0.11 ppb in winter and 4.4 ppb in summer, which remains small compared to the measurement uncertainties (1 ppb for in situ data and 6 ppb for TCCON) and the magnitude of the observed bias. Moreover, the higher impact in summer should theoretically cause a model overestimation during this season when the OH sink is ignored. However, since the observed seasonal bias shows a different trend, it is unlikely to be driven by CH_4 chemistry.

Therefore, our analysis highlights an urgent need for further research into the seasonality of CH_4 emissions in northern China.

3.4 Impact of meteorology on variability of concentrations

In Sect. 3.2, we showed how emissions from different sources affect the CH_4 observations at Xianghe. In the current section we want to focus on the meteorological factors that influence the temporal variability of the time series. More specifically we will discuss the impact of large-scale phenomena, the planetary boundary layer and local winds.
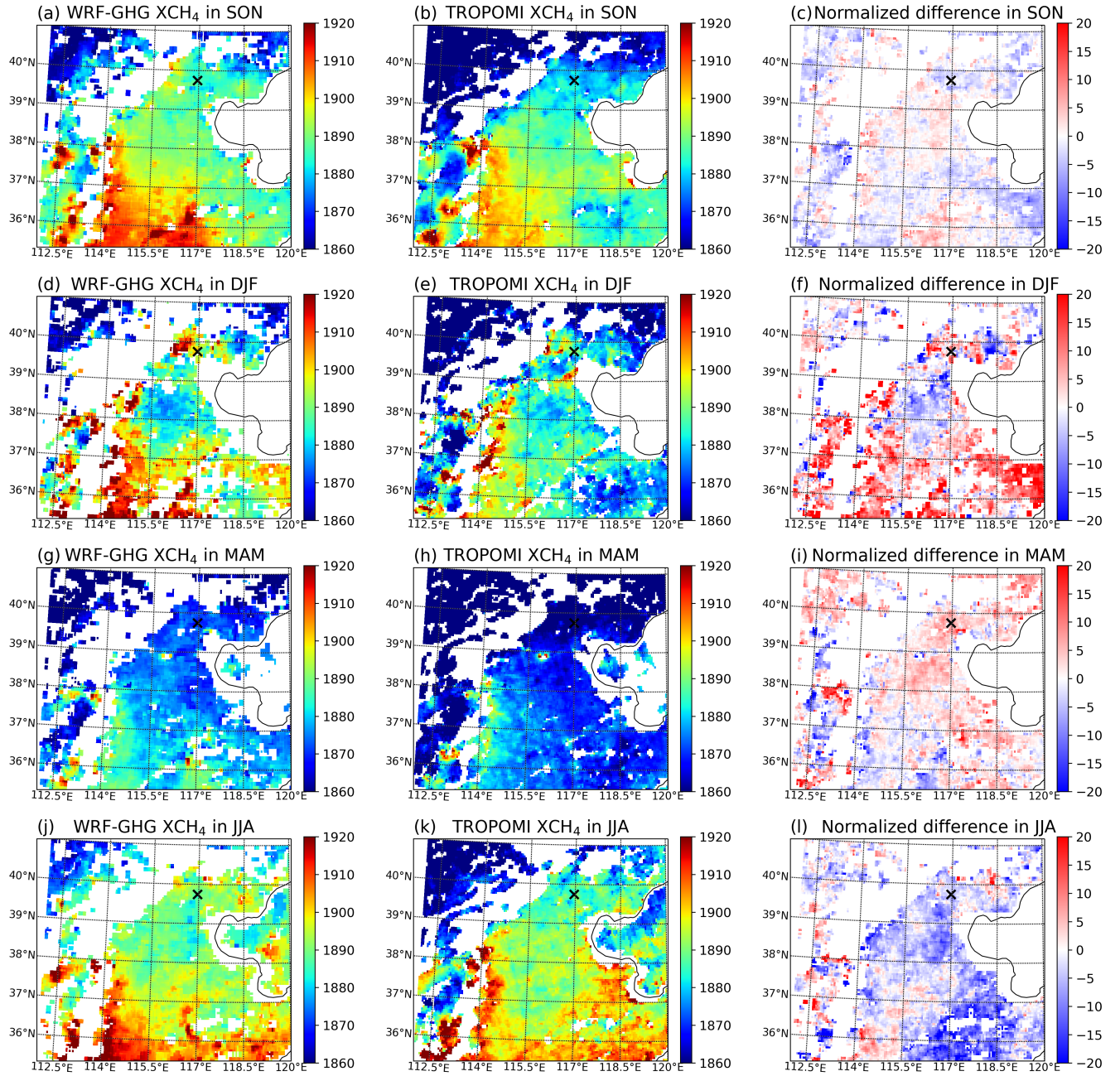
Figure 7. Seasonal mean XCH$_4$ (ppb) over the domain d02 (provinces of Beijing, Tianjin, Hebei, Shanxi and part of Shandong) as simulated by WRF-GHG (first column) and observed by TROPOMI (second column), as well as the normalized difference between them (WRF-GHG - TROPOMI, in ppb). Normalized difference indicates that the mean difference over the entire simulation period is subtracted from the seasonal means. The seasons are defined as (a,b,c) SON: September - November (autumn), (d,e,f) DJF: December - February (winter), (g,h,i) MAM: March - April (spring) and (j,k,l) JJA: June - August (summer). White pixels indicate that there are no observations available during the entire period.

3.4.1 Synoptic scale winds

Because FTIR observations generally have a large area of representativeness (generally a few 100 km), column concentrations are relatively insensitive to local fluxes and vertical mixing, while they are strongly influenced by large-scale patterns (Keppel-Aleks et al., 2011). We use the winds at 800 hPa to represent horizontal transport in the free troposphere, as this altitude is generally above the planetary boundary layer height. More specifically, we looked at the daily mean column concentrations above the background for every wind direction to see if a clear relationship could be found. This is shown in Fig. 8.

Remark that only southwest (SW) and northwest (NW) wind segments are given because southeast and northeast winds occur only seldom at 800 hPa: only on 2 and 13 days out of 231, respectively. We find that in general, larger enhancements are found when winds blow from the SW wind segment (median tracer contribution of 57.79 ppb) compared to the NW segment (median tracer contribution of 7.33 ppb). To quantify the difference, we conducted a non-parametric Mann-Whitney U test on the two categories, which yielded p-values well below 0.05 (see Fig. 8, in the title), indicating that the differences are statistically significant. Higher concentrations coincide with 800 hPa winds coming from the SW while NW winds correspond with lower concentrations. Yang et al. (2020) already showed that the day-to-day variation of the column observations of CH_4, CO_2 and CO are highly intercorrelated, and that clean days are linked with air from the north, while polluted days are linked with air from the south, which is confirmed here by the WRF-GHG simulations. Air masses from the north have been moving over rather remote and clean areas such as Inner Mongolia, Mongolia and Russia. Meanwhile, southerly air is linked with the highly populated North China Plain (NCP), where many anthropogenic emission sources are located.

The influence of polluted air from the southwest is visible in the surface concentrations as well, as we find a high correlation coefficient of 0.79 between the daily mean column and surface tracer enhancements. This indicates that both surface and column CH_4 concentrations are affected by synoptic-scale winds, which advect either clean or polluted air masses to Xianghe. Furthermore, the levels of pollution in these air masses can vary significantly from month to month due to changing meteorological conditions. For instance, during the winter months, weather conditions are generally more favorable to the accumulation of pollutants, leading to higher pollution levels (Li et al., 2022). This can intensify both local pollution plumes and those transported by southwestern winds. This phenomenon likely explains why despite relatively constant emissions throughout the year, we observe a significant month-to-month variability in the energy tracer contributions (see Fig. 5). More specifically, we find a CV of 26.53% for the column and 26.65% for the surface tracers. These findings suggest that tracer concentrations at Xianghe result from a complex interplay of emissions, wind direction, and weather patterns both near and far.

3.4.2 Planetary boundary layer dynamics

The planetary boundary layer (PBL) is the lowermost layer of the atmosphere which is in direct contact with the Earth's surface. The characteristics of this layer vary throughout the day. During the day, under influence of solar radiation, turbulent motions cause strong vertical mixing of the air within the PBL. These processes allow gases to be dispersed and transported upwards, which generally leads to reduced concentrations near the surface. At night, radiational cooling of the surface creates
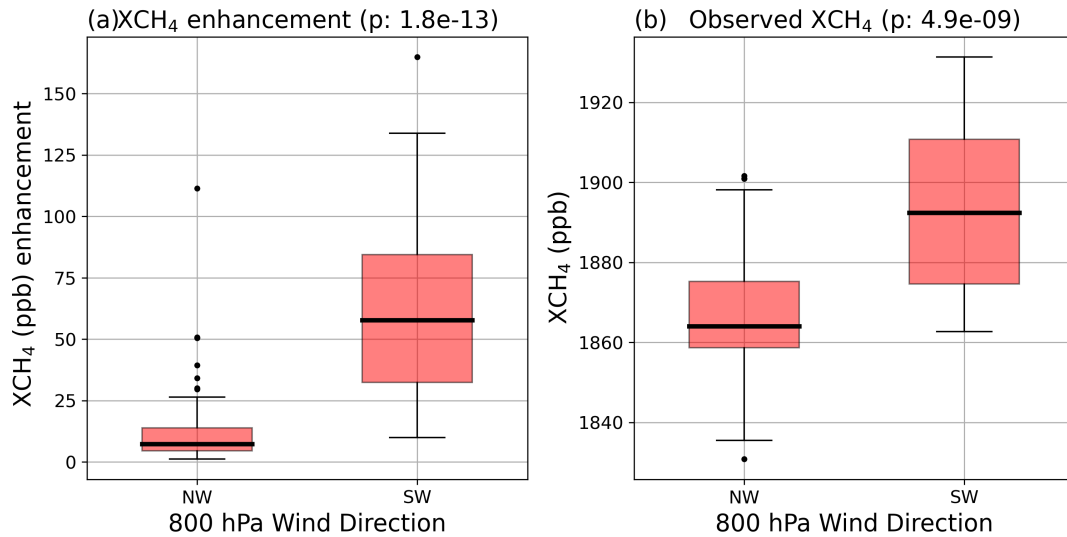
Figure 8. Distribution of the daily mean (a) simulated column tracer above the background and (b) observed XCH_4 per 800 hPa wind direction category. NW is for winds with an angle of 292.5 to 337.5 $^\circ$ from north, while SW represents the angles between 202.5 and 247.5 $^\circ$. There are 72 days with NW winds and 33 days with SW winds. The colored boxes indicate the range between the first and third quartile, while the thick solid line is the median. Outliers (values that are 1.5 times the interquartile range above (below) the third (first) quartile) are shown by black dots. The p-values of the corresponding non-parametric Mann-Whitney U tests are given in the title.

a temperature inversion close to the ground. This causes the nocturnal PBL to be stable and more shallow, trapping pollutants near the surface and as such increasing their local concentrations.

Figure 9 shows the diurnal variation of the PBL height as simulated by WRF-GHG and the CH_4 concentrations near the surface (both simulated and observed). Indeed, the height of the PBL in WRF-GHG is largest in the afternoon when solar radiation is strongest, reaching its peak at 15:00 (local time). This corresponds with the lowest simulated surface concentrations (Fig. 9b), where we find median (and interquartile) values of 2039.77 (1977.74 - 2158.28) ppb. Right after sunset, the height of the PBL drops to its lowest value ($\approx$ 50 m - 430 m in WRF-GHG), after which it persists during the course of the night, until sunrise. This period corresponds with slightly increasing CH_4 concentrations as emissions near the surface accumulate within this stable shallow layer. Hence, the highest concentrations are found in the early morning: at 8:00 with 2239.75 (2079.29 - 2484.04) ppb. As the PBL height starts to rise at 8:00 due to turbulent mixing, CH_4 start to drop in WRF-GHG, creating a diurnal cycle.

Note that WRF-GHG is quite capable at simulating this diurnal variation of CH_4 in situ observations. The observations show minimal concentrations at 16:00 with a median (and interquartile) value of 2041.94 (1981.54 – 2135.88) ppb, which are well captured by WRF-GHG, even though one hour earlier. The peak CH_4 concentrations however, are observed at 6:00 with a median (and interquartile) value of 2252.71 (2104.36 – 2451.01) ppb, portraying a small model underestimation of about 13 ppb. Together, this leads to a small underestimation of the CH_4 diurnal amplitude in WRF-GHG of 10.79 ppb.
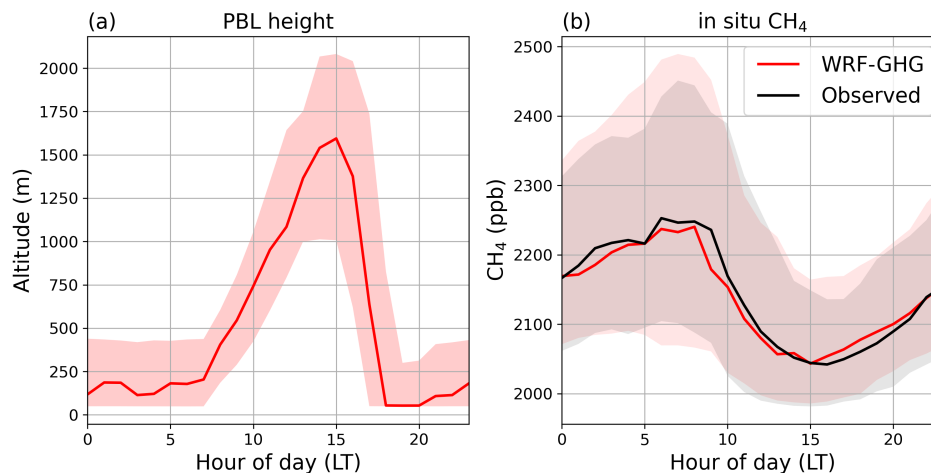
Figure 9. Hourly median and interquartile range of the (a) simulated planetary boundary layer height, and (b) observed and simulated surface CH$_4$ concentration at Xianghe.

We have shown that these PBL dynamics are very important for the variability of the surface concentrations, however they are irrelevant for the column concentrations, as the latter are much less affected by vertical transport (Wunch et al., 2011). Indeed, the WRF-GHG simulated column concentrations don't exhibit a clear diurnal cycle, suggesting that this aspect is well captured by the model. It is however difficult to validate this using observations, as FTIR measurements are only possible during periods of sunlight.

3.4.3 Local emissions

Regional emissions are influencing both column and in situ concentrations at Xianghe, as elaborated in Sect. 3.4.1. However, emission sources nearby could also have an impact on these values, especially for the in situ observations as they sample the local air. To analyze which nearby sources influence the Xianghe measurements, we look for correlations between the 10m wind direction and the simulated concentrations. Figure 10 reveals the mean WRF-GHG tracer contribution per wind direction for CH$_4$. To eliminate the influence of polluted plumes from further away, we select only those days on which the mean daily XCO enhancement is smaller than 45 ppb. We use XCO as a tracer for polluted events as it is the species with the shortest atmospheric lifetime. Furthermore, we compute the mean concentrations separately for day and night to avoid the effects of the PBL. The night hours are defined as those with the peak concentrations, i.e., between 3h and 8h LT, while the day represents those hours with highest atmospheric mixing and lowest concentrations, i.e., between 13h and 18h. During the day most winds are coming from the north and southwest, while at night the most frequent wind directions near the surface are north and east. Corresponding panels indicating the frequency of wind speed per direction is given in Fig. C1. We find higher wind speeds during the day than at night. The northern winds typically have the lowest tracer contributions since there are fewer emission sources in this direction, with the exception of agriculture (see Fig. 11). In general, we see that wind directions with the largest
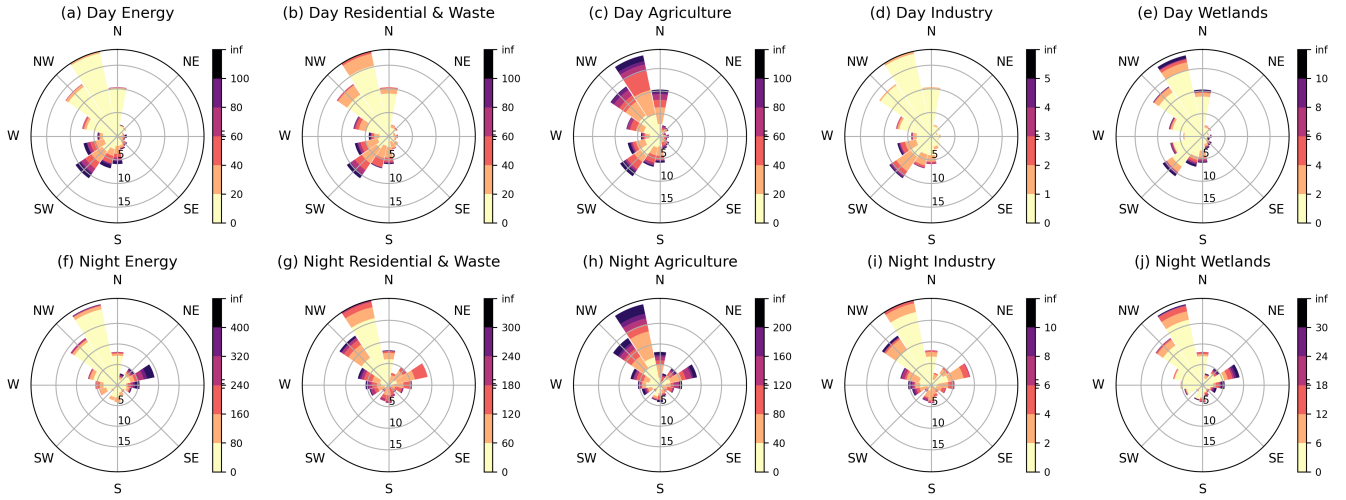
Figure 10. Mean CH$_4$ simulated tracer concentrations (ppb) binned per wind direction for the main sectors (a) energy, (b) residential & waste, (c) agriculture, (d) industry and (f) wetlands on days without strong regional pollution. The lengths of the bars show the frequency of any wind direction binned by 22.5 °, given in percentage. The first row represents afternoon hours (13h - 18h LT), while the second row represents nighttime hours (3h - 8h LT). Remark that the panels have different concentration bins.

enhancements correspond with the largest sources nearby (Fig. 10-11): east and west for energy, all but north for residential, all directions for agriculture, southwest for industry and east-southeast for wetlands. The highest values overall (> 400 ppb) are found for the energy tracer at night and they are coming from the east, where some very large CH$_4$ point sources are located that correspond to coal mine emissions nearby the city of Tangshan (see Fig. 11a). However, when looking closer at the CH$_4$ time series (not shown) we see that WRF-GHG is often overestimating the Xianghe in situ CH$_4$ observations at times where the model shows a large energy contribution. This is also visible in Fig. 12. This makes us to believe that these coal mine emissions might be overestimated in CAMS-GLOB-ANT. In the next section we further investigate this hypothesis by comparing WRF-GHG concentration fields with TROPOMI observations.

3.5 Source assessment near Tangshan

By comparing the yearly TROPOMI XCH$_4$ with WRF-GHG XCH$_4$, we want to assess if the CH$_4$ emissions from coal mines around Tangshan are indeed overestimated in CAMS-GLOB-ANT or not. Figure 13 shows the maps of the mean XCH$_4$ during the entire simulation period: September 2018 until September 2019. The yearly mean total CH$_4$ fluxes from CAMS-GLOB-ANT in the WRF-GHG d02 is also given, as well as the difference between WRF-GHG and TROPOMI. By taking the average over the complete simulation period we minimize the influence of meteorological patterns on the XCH$_4$ concentration and expose the main emission sources.

When comparing the WRF-GHG input fluxes in Fig. 13a with the resulting XCH$_4$ concentration field in Fig. 13b, we indeed

Mean CH$_4$ flux (mol km^{-2} h^{-1})
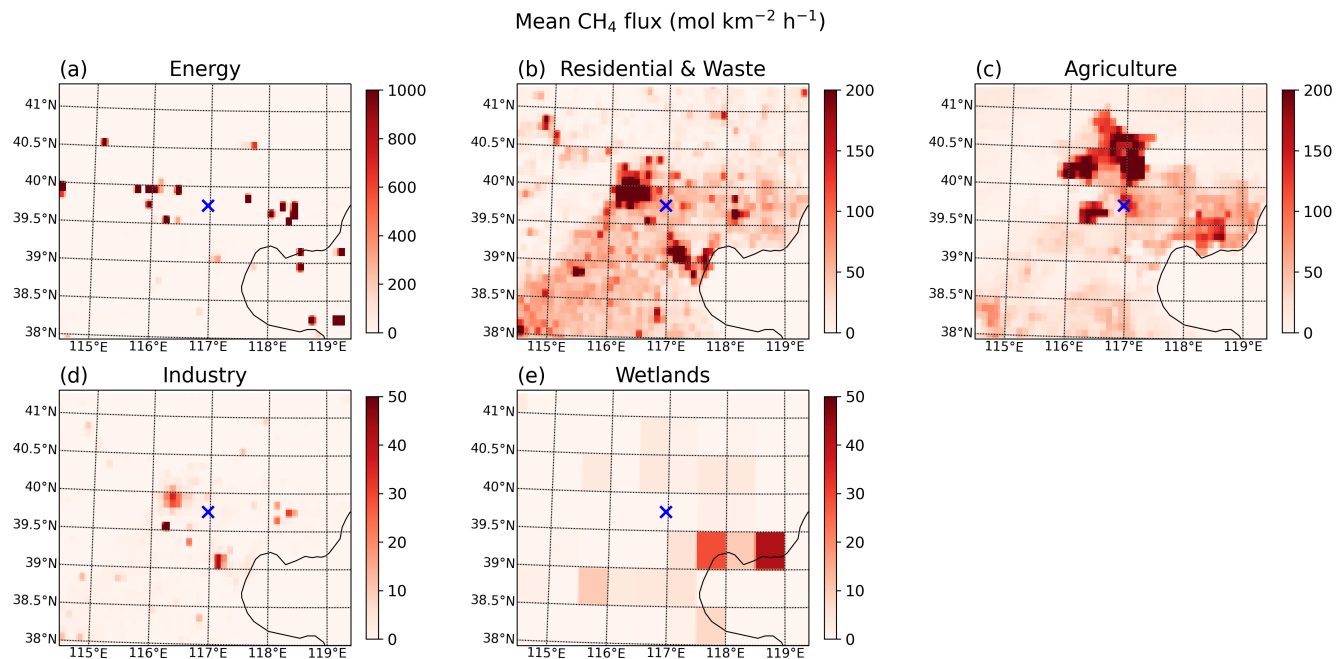
Figure 11. Map of the mean CH$_4$ flux (mol km^{-2} h^{-1}) in WRF-GHG domain d03 during the entire simulation period from September 2018 until September 2019, for the most important sectors. Remark that the panels have different color scales. The location of the Xianghe site is indicated by a blue cross.
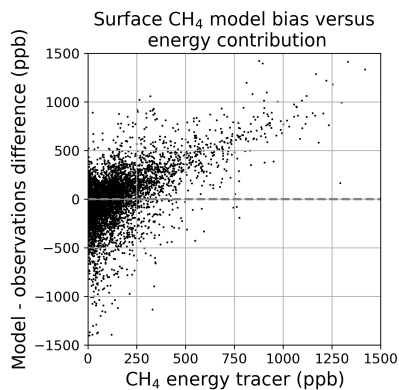
Figure 12. Correlation between energy tracer contribution to simulated CH$_4$ surface concentrations and differences between total simulated and observed surface concentrations. For this plot, the data was not filtered on day, night or polluted/clean days.

find a strong agreement. The largest sources are found to the west of 114°E, which correspond to the extensive coal mining activities in Shanxi. In the same locations on the XCH_4 map of WRF-GHG we find the highest concentration values of the region. Unfortunately due to the mountainous terrain, TROPOMI observations are sparse in this area. Other sources, such as a hotspot around 36.25°N, 116.75°E and the slightly smaller emissions around Beijing (40°N, 116.3°E) and Tangshan (39.6°N, 118.4°E) correspond with elevated XCH_4 values. This suggests that yearly averaged XCH_4 maps can indeed reveal the strongest emission sources. It should be noted however, that the CH_4 sources around Beijing and Tangshan are approximately three times smaller than those in Shanxi (west of 114°E) and are barely strong enough to cause significant enhancements in the yearly XCH_4 maps. Our analysis indicates that point sources should emit at least around 0.1 Tg per year to be clearly distinguishable on annual XCH_4 maps, taken into account the noise of the observations. The region below 37°N shows high simulated XCH_4 values as well, however they do not directly correspond to strong sources in the inventory. This can likely be explained by the presence of the Taihang mountains on the west which lead to poor dispersion conditions (Fu et al., 2014). Therefore the larger concentrations in this area are likely more determined by the topography and associated meteorological conditions than by surface fluxes.

We observe slightly elevated XCH_4 values near the coal mines of Tangshan in both the WRF-GHG and TROPOMI maps. To isolate the potential model bias over these sources, we defined a surrounding background region (39.3-40 °N, 117.8-118.8 °E), characterized by the absence of major CH_4 emissions, and a source region (39.45-39.8 °N, 118.15-118.6 °E) encompassing the concentrated coal mine sources from CAMS-GLOB-ANT. The mean difference (WRF-GHG - TROPOMI) was 8.87 ± 2.22 ppb in the background region and 11.85 ± 3.24 ppb over the source region, suggesting a potentially larger model overestimation near the coal mines. However, when considering the reported spatial variability of the TROPOMI bias, this difference of approximately 3 ppb is not statistically significant. Validation studies by the S5P Mission Performance Centre (MPC) indicate a bias dispersion of 0.7% across different FTIR sites, which translates to a potential bias variation exceeding 13 ppb. Therefore, based on this TROPOMI comparison alone, we cannot definitively conclude that the CAMS-GLOB-ANT emissions from these sources are overestimated. Additional in situ CH_4 measurements in the immediate Tangshan area are crucial for a more robust assessment.

Note that the XCH_4 maps in Fig. 13 suggest that it is very likely that the CH_4 hotspot around 36.25°N, 116.75°E is overestimated as well, as the very strong XCH_4 enhancement in WRF-GHG is absent in the TROPOMI map.

4 Conclusions

We have used the WRF-Chem model in its greenhouse gas option WRF-GHG to simulate surface concentrations and column abundances of CO_2, CH_4 and CO observed at the Xianghe site in China, aiming to improve our understanding of the variabilities in the measured time series. Since June 2018, column-averaged concentrations are measured with a FTIR spectrometer that is part of TCCON, while near-surface concentrations of CO_2 and CH_4 are measured with a PICARRO CRDS analyzer at an altitude of 60 m.a.g.l. We computed 3-D concentration fields from September 2018 until September 2019 in three nested domains covering a large part of China. The ground-based observations are compared with simulations from the
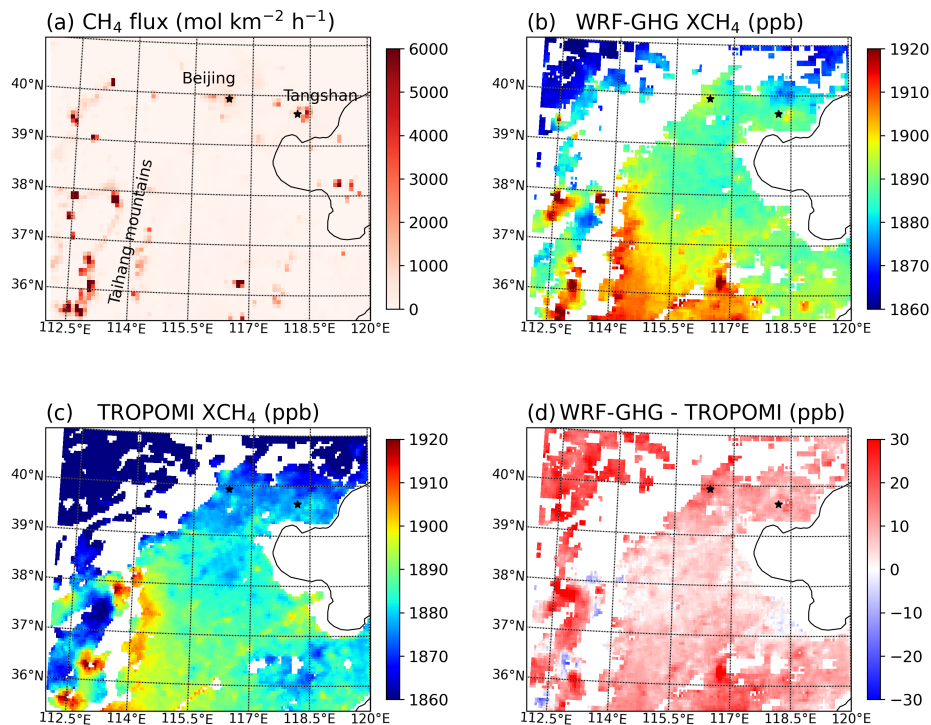
Figure 13. (a) The CH$_4$ flux from all sectors in CAMS-GLOB-ANT averaged from September 2018 until September 2019 and regridded to WRF-GHG grid d02 (9 km resolution). Mean XCH$_4$ over the same period as (b) simulated by WRF-GHG and (c) observed by TROPOMI (both regridded to 0.05 °). (d) Mean difference between WRF-GHG and TROPOMI XCH$_4$ over the entire simulation period.

460 innermost domain, centered on the Beijing-Tianjin-Hebei region, with a horizontal resolution of 3×3 km^2. We employed the CAMS-GLOB-ANT v5.3 inventory for anthropogenic emissions of CO$_2$ and CH$_4$, and the REAS v3.2.1 dataset for CO. To disentangle the total simulated signal into the various source sectors, including a wide range of both natural and anthropogenic sources, they were simulated as separate tracers. This study is the first part of the analysis, focusing on CH$_4$.

In general, the model demonstrated moderate performance, with a correlation coefficient of 0.66 for near-surface CH$_4$ concen-

465 trations in the afternoon and 0.56 for column-averaged concentrations. After adjusting for the observed seasonal bias coming from the boundary conditions (CAMS reanalyses), the performance improved, as indicated by an increase in the correlation coefficient to 0.67 with the TCCON time series.

The simulated CH$_4$ concentrations is predominantly influenced by emissions from three main human activity sectors: energy, residential & waste, and agriculture. The energy sector has a more significant impact on column abundances (accounting for

470 52.9% of the total enhancement) compared to surface concentrations (36.9%), reflecting differences in the sensitivity of remote sensing and in situ measurements to sources at large distances, such as Shanxi province. For the in situ concentrations, the three emission sectors are equally important.

Monthly variability in the contributions from each tracer is found to align broadly with expected emission patterns: the residen-

tial tracer is higher in winter, while the agricultural tracer peaks in late summer (September). This month-to-month variation is further influenced by meteorological conditions such as horizontal advection and atmospheric stability, which is especially visible in the energy tracer where corresponding emissions remain relatively constant throughout the year, while the contributions from this tracer show notable variations.

The model simulations confirm the importance of large-scale wind patterns, with air masses from the southwest transporting higher CH_4 concentrations to the Xianghe site compared to those from the northwest (median tracer contributions of 57.8 ppb vs. 7.3 ppb, respectively). During southwest wind regimes, pollution from the densely populated North China Plain reaches the Xianghe site. While large-scale air masses influence the variability of both measurement types, smaller-scale factors such as planetary boundary layer dynamics and local wind patterns, also play a significant role for the near-surface concentrations. WRF-GHG effectively captures the diurnal variability driven by these boundary layer dynamics, with CH_4 surface concentrations reaching their lowest levels in the afternoon (16:00 LT) and peaking around sunrise (6:00 LT), leading to a diurnal amplitude of almost 200 ppb.

Despite correcting for the bias in boundary conditions, a residual seasonal bias remained in the model, likely due to inaccuracies in emission estimates from agricultural (livestock) and waste management activities. Furthermore, comparisons between simulated and observed CH_4 concentrations near the surface, suggest an overestimation of coal mine emissions near Tangshan in the emission inventory of CAMS-GLOB-ANT. However, this hypothesis remains unconfirmed due to the averaging effect in the column measurements, the relatively low emission strength and the reported accuracy of TROPOMI XCH_4.

In summary, the WRF-GHG model successfully captures key aspects of CH_4 variability at the Xianghe site for both remote sensing and in situ observations. The model simulations also provide valuable insights into the relative contributions of different source sectors and the influence of meteorological processes on CH_4 concentrations.

However, the observed discrepancies, particularly the seasonal bias and overestimated emissions from certain sources, underscore the need for improved emission inventories in this region of China, especially for agricultural, waste management, and coal mining activities. Future research should aim to enhance our understanding of the monthly variations of CH_4 in northern China, which is crucial for providing more accurate boundary conditions and emission flux information to high-resolution modeling studies like the present work. By addressing these challenges, we can further refine our understanding of CH_4 sources and their impacts on regional air quality, ultimately contributing to more effective greenhouse gas mitigation strategies.

Code and data availability. The ERA5 and CAMS reanalysis data set (Hersbach et al., 2023a, b), used as input for the WRF-GHG simulations, was downloaded from the Copernicus Climate Change Service (C3S) Climate Data Store (2022). The CAMS-GLOB-ANT v5.3 emissions (Granier et al., 2019; Soulie et al., 2023) and temporal profiles CAMS-GLOB-TEMPO v3.1 (Guevara et al., 2021) are archived and distributed through the Emissions of atmospheric Compounds and Compilation of Ancillary Data (ECCAD) platform. The REAS emission inventory is publicly available at https://www.nies.go.jp/REAS/ (Kurokawa and Ohara, 2020). The WRF-Chem model code is distributed by NCAR (https://doi.org/10.5065/D6MK6B4K, NCAR, 2020). The WRF-GHG simulation output created in the context of this study can be accessed on https://doi.org/10.18758/P34WJEW2 (Callewaert, 2023). The TCCON data were obtained from the TCCON Data Archive hosted by CaltechDATA at https://tccondata.org (Zhou et al., 2022), while the surface observations at Xianghe were received through private com-

Table A1. Overview of sensitivity tests on different physical parameterization options. They are a combination of three different PBL schemes: Yonsei University (Hong et al., 2006), Mellor-Yamada-Janjic (Janjić, 1994) and Mellor-Yamada-Nakanishi Niino Level 3 (Nakanishi and Niino, 2006, 2009; Olson et al., 2019); two surface layer schemes: Revised MM5 (Jiménez et al., 2012) and Eta similarity (Janjić, 1994); and two radiation schemes: RRTMG Longwave and Shortwave schemes (Iacono et al., 2008) versus RRTM Longwave and Dudhia Shortwave schemes (Dudhia, 1989; Mlawer et al., 1997).

Test	PBL	Surface Layer	Radiation
BASE	YSU scheme (option 1)	Revised MM5 scheme (option 1)	RRTM and Dudhia (option 1)
A	YSU scheme (option 1)	Revised MM5 scheme (option 1)	RRTMG (option 4)
B	MYJ scheme (option 2)	Eta similarity scheme (option 2)	RRTMG (option 4)
C	MYNN3 scheme (option 6)	Eta similarity scheme (option 2)	RRTMG (option 4)
D	MYNN3 scheme (option 6)	Revised MM5 scheme (option 1)	RRTMG (option 4)

munication with the co-authors. TROPOMI Level 2 Methane Total Column data are publicly available online at https://doi.org/10.5270/S5P-3lcdqiv and the Copernicus Open Access Hub.

Appendix A: WRF-GHG sensitivity tests

Sensitivity tests were carried out to identify a model configuration that matches the observations (of CO_2, CH_4 and CO) well. We have tested several physical parameterization schemes and anthropogenic fluxes because these elements are essential to accurately simulate tracer concentrations. The initial set of physical parameterization schemes (BASE) was taken from Li et al. (2020) and Dong et al. (2021) as they have shown good model performance for simulating CO_2 concentrations in China. Four alternative combinations (A-D) were created by changing the schemes for the longwave and shortwave radiation, planetary boundary layer (PBL) and surface layer physics, leading to 5 different model configurations in total (see Table A1). Remark that there are several more physical parameterization schemes that could have been included in these tests. Nevertheless, a full sensitivity analysis is outside the scope of this study. Thus, we restricted our tests to the most frequently used schemes in the literature and chose the combination that produced satisfactory model simulations without additional optimization.

Further, the following anthropogenic flux inventories were tested: EDGAR GHG v6.0 (for CO_2 and CH_4, Ferrario et al. (2021)), EDGAR Air Pollutants v5.0 (for CO, Crippa et al. (2019)), CAMS-GLOB-ANT v5.3 (for CO_2, CH_4 and CO, Granier et al. (2019); Soulie et al. (2023)), PKU v2 (for CO_2 and CO, Wang et al. (2013); Zhong et al. (2017)), REAS v3.2.1 (for CO_2 and CO, Kurokawa and Ohara (2020)), MEICv3.1 (for CO_2 and CO, http://www.meicmodel.org/), ODIAC2020b (for CO_2, Oda and Maksyuto (2011, 2020); Oda et al. (2018)) and FFDAS v2.2 (for CO_2, Asefi-Najafabady et al. (2014)). Monthly fluxes are disaggregated into hourly fluxes using the temporal factors of Crippa et al. (2020), Guevara et al. (2021) and Nassar et al. (2013). The model code was adapted to include these different anthropogenic emission inventories in separate tracers. As such, one simulation is sufficient to compare the effect of all inventories.

The five simulations, representing different combinations of physical parameterization schemes and anthropogenic fluxes, were run over three periods of about 2 weeks spread over the year: 1-17 October 2018, 1-17 February 2019 and 10-25 June 2019. The first 48h were regarded as spin-up and are not taken into account in the analysis.

For each time series the root mean square error (RMSE), mean bias error (BIAS) and Pearson correlation coefficient (CORR) were calculated. In order to find the most suitable combination of physical parameterization schemes and anthropogenic emission inventory for all observations at Xianghe, a combined skill score (S) was computed as follows, based on Gbode et al. (2019):

$$S = (1 - RMSE_{norm}) + (1 - |BIAS_{norm}|) + CORR_{norm}, \tag{A1}$$

where $X_{norm} = \frac{X_i - X_{min}}{X_{max} - X_{min}}$ is the normalized statistical metric. As such, the combination with the highest S will overall have the lowest RMSE, lowest absolute BIAS and highest CORR. Exact values of the statistical metrics and combined skill scores for every sensitivity test can be found below in Tables A2, A3, A4, A5 and A6 for the time series of in situ CO_2, in situ CH_4, XCO_2, XCH_4 and XCO, respectively.

Unfortunately, there is not one combination of physical parameterization schemes and anthropogenic flux inventories that yields optimal scores for all species (CO_2, CH_4 and CO) across various observation types (surface and column). To identify the most appropriate model configuration for simulating all observations at the Xianghe site, it is necessary that the chosen physical parameterization schemes (denoted as test A - D, BASE) show satisfactory skill scores across all five time series. Moreover, the choice of anthropogenic flux inventory, although potentially varying among species, should yield reasonable score values for all observation types of the same species. Therefore, the final combination was determined through the following logical process, where preference was given to the surface data (as it is assumed that the physical schemes will have the highest impact on these simulations):

- We reject the combination with the worst retults: for each statistical metric, we calculate a threshold derived from the mean (μ) and standard deviation (σ) of all occurring values. Combinations in which one or more of the metrics exceed or fall below these thresholds are excluded from the selection process. Specifically, these combinations must conform to the following set of equations:

$$\text{CORR} \geq \mu_{\text{CORR}} - \sigma_{\text{CORR}},$$
$$|\text{BIAS}| \leq \mu_{|\text{BIAS}|} + \sigma_{|\text{BIAS}|},$$
$$\text{RMSE} \leq \mu_{\text{RMSE}} + \sigma_{\text{RMSE}} \tag{A2}$$

The combinations that are discarded after this step are indicated with an asterisk (*) behind the inventories name in the tables below.

- For CO_2 and CH_4, discard the combinations that are only present in the table of either the surface or either the column data in order to keep only those that are performing good enough on both time series. The combinations that are discarded after this step are highlighted in italic in the tables below.

- From what is left, we see that only combinations with test A, B or C should be considered as those with test D and BASE settings have been discarded for CH_4. The choice of physical parameterization option should be the same for all species. When sorting the remaining combinations for CO_2 and CO based on S (from the in situ time series for CO_2), we find that options with test B and C are superior to those with test A. Finally, a choice has to be made between options with test B and options with test C.

- For both test B and C, we take the emission inventory which has the highest S, for CO_2 and CH_4 based on the in situ time series and for CO based on the column. This leads to the following options:

  - Test B: CAMS-GLOB-ANT for CH_4 and CO_2; REAS for CO

  - Test C: CAMS-GLOB-ANT for CH_4, REAS for CO_2 and PKU for CO

- The final choice between these two options is rather arbitrary since certain combinations yield slightly improved results for one time series but perform less favorably for another, and vice versa. In our study we have chose the combinations with test B.

This approach leads to the settings of test B, together with CAMS-GLOB-ANT v5.3 fluxes for CO_2 and CH_4 and REAS v3.2.1 (Regional Emission Inventory in Asia) fluxes for CO.

Appendix B: FLEXPART simulations

The FLEXPART v10.4 model (Pisso et al., 2019) is applied to quantitatively estimate the OH impact on the WRF-GHG CH_4 simulation at Xianghe. Table B1 lists the main settings of the FLEXPART model. CH_4 particles are released using the FLEXPART backward mode at Xianghe site with and without OH reaction. We release the CH_4 particles between 00:00-01:00 and 12:00-13:00 (LT) every day in Oct 2018, Jan 2019, Apr 2019 and July 2019. The release height is set to 0-100 m a.g.l., since the OH reaction will have a higher impact near the surface where the wind is weaker than at higher altitudes. The backward running duration is set to 3 days, and the backward sensitivities are extending outside of the WRF-GHG d01 boundary. As an example, Fig. B1 shows the spatial distribution of CH_4 backward sensitivities for a release at 12:00-13:00 LT on 30 January 2019 including the OH reaction, and Fig. B2 shows the corresponding relative difference in the CH_4 backward sensitivities between the simulations with and without OH reaction. Note that FLEXPART v10.4 includes a monthly OH climatology based on GEOS-Chem simulations (Pisso et al., 2019).

Appendix C: Additional figures

Figure C1 shows a wind rose of simulated wind speed and direction at Xianghe, accompanying Figure 10 in section 3.4.3.

Table A2. Statistical metrics for sensitivity tests, in situ CO_2 data at Xianghe. Unit of BIAS and RMSE is ppm. Rows where the inventory name if followed by an asterisk ($*$) indicate those where one or more statistical metrics surpass the thresholds defined in Eq. A2. Rows in italic represent combinations that are rejected due to the XCO_2 value falling outside the thresholds. The bold lines represent the final two options as determined by the methodology outlined in Appendix A.

Test	Flux	CORR	BIAS	RMSE	S
B	*PKU*	*0.67*	*-1.62*	*16.09*	*2.91*
B	**CAMS**	**0.63**	**-0.12**	**17.50**	**2.81**
B	EDGAR	0.63	0.92	17.87	2.72
C	*PKU*	*0.64*	*-3.96*	*16.91*	*2.65*
C	**REAS**	**0.61**	**-1.19**	**18.88**	**2.58**
A	*PKU*	*0.63*	*-4.51*	*17.16*	*2.57*
BASE	*PKU*	*0.61*	*-3.51*	*17.65*	*2.53*
D	*PKU*	*0.62*	*-4.84*	*17.38*	*2.52*
C	FFDAS	0.58	-0.92	19.12	2.50
C	CAMS	0.59	-2.77	18.06	2.49
C	EDGAR	0.58	-1.71	18.53	2.47
D	FFDAS	0.58	-1.69	19.19	2.44
B	REAS	0.58	1.44	20.14	2.41
B	FFDAS	0.60	2.97	20.19	2.41
A	CAMS	0.58	-3.46	18.26	2.40
A	EDGAR	0.57	-2.46	18.58	2.40
A	FFDAS	0.56	-1.36	19.76	2.35
C	MEIC	0.63	5.15	20.68	2.34
D	CAMS	0.57	-3.74	18.90	2.30
D	EDGAR	0.55	-2.73	19.32	2.29
BASE	REAS	0.55	-0.29	22.00	2.27
A	REAS	0.55	-1.33	21.49	2.25
A	*MEIC*	*0.59*	*4.60*	*21.84*	*2.20*
D	MEIC	0.58	4.02	21.86	2.19
D	REAS	0.54	-1.33	22.02	2.19
BASE	FFDAS $*$	0.51	0.11	21.66	2.17
BASE	CAMS $*$	0.52	-2.21	20.93	2.13
BASE	EDGAR $*$	0.51	-1.11	21.72	2.09
B	MEIC $*$	0.64	9.16	22.95	2.07
BASE	MEIC $*$	0.57	5.94	23.34	1.99
D	ODIAC $*$	0.52	3.63	22.57	1.96
C	ODIAC $*$	0.53	5.04	22.80	1.91
A	ODIAC $*$	0.49	4.56	24.46	1.69
B	ODIAC $*$	0.54	8.63	24.91	1.63
BASE	ODIAC $*$	0.47	5.81	25.67	1.51

Table A3. Same as Table A2 but for in situ CH_4. Unit of BIAS and RMSE is ppb.

Test	Flux	CORR	BIAS	RMSE	S
C	**CAMS**	**0.52**	**2.19**	**206.50**	**2.81**
C	EDGAR	0.52	19.09	208.24	2.67
BASE	*CAMS*	*0.48*	*3.26*	*213.26*	*2.47*
A	*CAMS*	*0.45*	*-7.09*	*210.84*	*2.31*
BASE	*EDGAR*	*0.48*	*22.33*	*216.09*	*2.28*
A	EDGAR	0.46	12.50	213.59	2.27
B	**CAMS**	**0.50**	**31.39**	**228.56**	**2.17**
B	EDGAR [*]	0.51	52.53	237.75	1.87
D	EDGAR [*]	0.41	8.83	237.26	1.70
D	CAMS [*]	0.39	-9.19	237.31	1.60
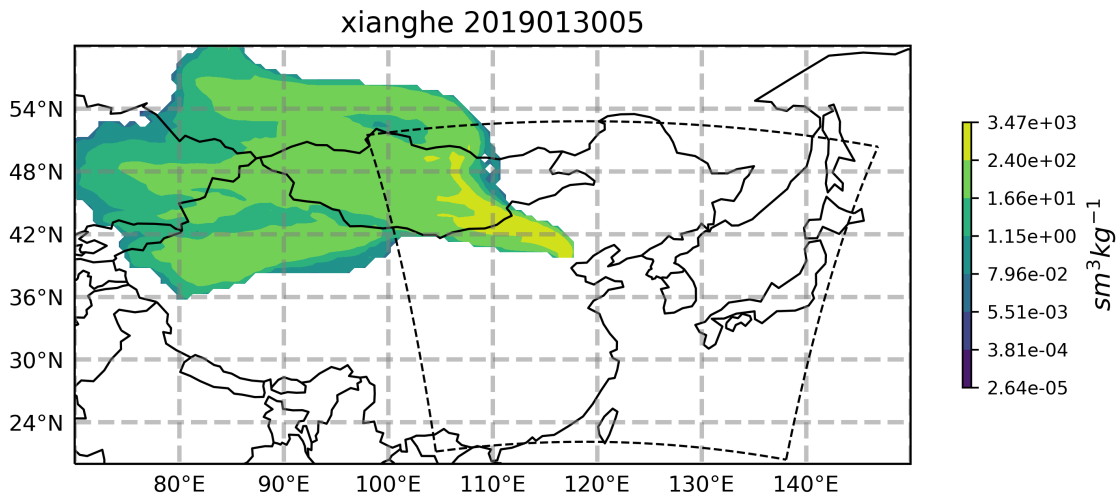
Figure B1. The spatial distribution of CH_4 backward sensitivities (in sm^3kg^{-1}) for a release at 12:00-13:00 LT (which is 04:00-05:00 UTC as indicated in the title) on 30 January 2019 from the FLEXPART simulation including the OH reaction. The location of WRF-GHG d01 is indicated by the dashed line.

Author contributions. SC made the model simulations and performed the formal analysis, investigation and visualization. The research was conceptualized by SC, MDM and EM and supervised by MDM and EM. MZ, TW and PW have provided the observational in situ data at Xianghe. BL supported with computing tools to correctly compare the model with TCCON and TROPOMI data. MZ designed and performed the FLEXPART simulations. SC prepared the initial draft of this manuscript while it was reviewed and edited by MZ, BL, TW, MDM, EM and PW.

590

Table A4. Same as Table A2 but for XCO_2.

Test	Flux	CORR	BIAS	RMSE	S
D	MEIC	0.77	0.62	1.52	2.87
C	MEIC	0.76	0.62	1.54	2.83
BASE	MEIC *	0.66	0.95	1.95	1.86
D	*ODIAC*	*0.78*	*-1.27*	*2.28*	*1.86*
C	*ODIAC*	*0.79*	*-1.32*	*2.29*	*1.85*
A	MEIC *	0.62	0.97	2.03	1.62
D	FFDAS	0.80	-1.60	2.43	1.58
C	FFDAS	0.80	-1.62	2.45	1.55
BASE	*ODIAC*	*0.75*	*-1.36*	*2.47*	*1.54*
D	EDGAR	0.79	-1.59	2.45	1.54
A	*ODIAC*	*0.74*	*-1.30*	*2.50*	*1.49*
B	*ODIAC*	*0.72*	*-1.23*	*2.53*	*1.47*
C	EDGAR	0.77	-1.57	2.49	1.45
D	CAMS	0.79	-1.70	2.52	1.38
B	EDGAR	0.76	-1.54	2.55	1.38
B	FFDAS	0.75	-1.52	2.58	1.33
C	**REAS**	**0.80**	**-1.81**	**2.56**	**1.33**
BASE	*FFDAS*	*0.77*	*-1.65*	*2.58*	*1.32*
D	REAS	0.79	-1.80	2.56	1.32
BASE	*EDGAR*	*0.77*	*-1.64*	*2.59*	*1.31*
C	CAMS	0.77	-1.68	2.57	1.30
A	FFDAS	0.76	-1.62	2.60	1.28
B	**CAMS**	**0.75**	**-1.64**	**2.63**	**1.22**
BASE	*CAMS*	*0.76*	*-1.74*	*2.66*	*1.15*
D	PKU *	0.80	-1.98	2.67	1.13
C	PKU *	0.80	-2.00	2.67	1.13
B	REAS	0.75	-1.71	2.69	1.10
A	EDGAR	0.72	-1.54	2.71	1.09
BASE	REAS	0.76	-1.85	2.73	1.03
A	CAMS	0.72	-1.65	2.76	0.98
A	REAS	0.75	-1.84	2.75	0.97
B	MEIC *	0.55	1.25	2.30	0.95
B	PKU *	0.76	-1.91	2.77	0.94
BASE	PKU *	0.77	-2.02	2.81	0.87
A	PKU *	0.76	-2.00	2.82	0.84

Table A5. Same as Table A2 but for XCH$_4$. Unit of BIAS and RMSE is ppb.

Test	Flux	CORR	BIAS	RMSE	S
B	**CAMS**	**0.69**	**-0.79**	**20.53**	**2.94**
B	*EDGAR*	*0.69*	*0.65*	*20.94*	*2.62*
C	EDGAR	0.67	-0.96	21.24	1.73
D	*EDGAR*	*0.66*	*-0.80*	*21.45*	*1.47*
C	**CAMS**	**0.67**	**-2.16**	**21.31**	**1.12**
A	EDGAR	0.65	-1.17	21.72	0.86
BASE	EDGAR *	0.65	-1.66	21.76	0.59
D	CAMS *	0.65	-2.09	21.75	0.55
A	CAMS *	0.65	-2.75	21.45	0.37
BASE	CAMS *	0.65	-3.03	21.42	0.34
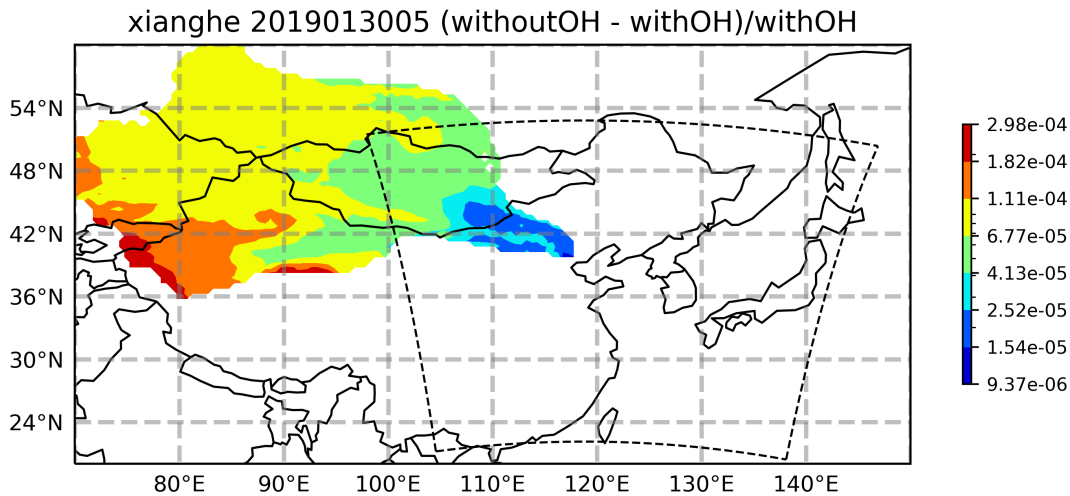
Figure B2. Relative difference in the CH$_4$ backward sensitivities between simulations with and without OH reaction. The location of WRF-GHG d01 is indicated by the dashed line.

Competing interests. The contact authors have declared that neither they nor their co-authors have any competing interests.

Disclaimer. The results contain modified Copernicus Climate Change Service information 2022. Neither the European Commission nor ECMWF is responsible for any use that may be made of the Copernicus information or data it contains.

Table A6. Same as Table A2 but for XCO. Unit of BIAS and RMSE is ppb.

Test	Flux	CORR	BIAS	RMSE	S
B	**REAS**	**0.78**	**-3.99**	**30.25**	**2.96**
B	PKU	0.78	-5.38	30.32	2.94
D	REAS	0.76	-5.32	31.54	2.83
BASE	REAS	0.77	-7.12	31.39	2.81
C	**PKU**	**0.76**	**-6.88**	**31.73**	**2.79**
D	PKU	0.76	-6.82	31.75	2.79
C	REAS	0.75	-5.53	32.00	2.79
BASE	PKU	0.77	-7.85	31.74	2.77
A	REAS	0.75	-7.15	32.35	2.72
A	PKU	0.75	-7.51	32.67	2.71
B	CAMS	0.68	-24.21	43.48	1.70
BASE	CAMS	0.66	-25.16	44.35	1.61
D	CAMS	0.64	-24.34	44.34	1.57
BASE	EDGAR [*]	0.52	3.27	57.84	1.45
A	CAMS	0.59	-23.19	44.78	1.44
C	CAMS	0.60	-23.77	45.07	1.43
B	EDGAR [*]	0.53	5.90	59.57	1.34
A	EDGAR [*]	0.50	6.27	62.83	1.16
D	MEIC [*]	0.65	-37.13	49.72	1.05
C	MEIC [*]	0.61	-37.10	50.26	0.94
B	MEIC [*]	0.53	-30.94	47.80	0.93
C	EDGAR [*]	0.46	8.30	67.22	0.87
D	EDGAR [*]	0.47	8.66	68.01	0.86
BASE	MEIC [*]	0.55	-34.80	49.89	0.82
A	MEIC [*]	0.52	-34.49	50.35	0.72

Table B1. The main settings of FLEXPART model run with a CH_4 tracer

Parameter	Settings
Release location	$\pm 0.1°$ around Xianghe site
Release height	0 - 100 m.a.g.l
Release time	00:00-01:00 and 12:00-13:00 (LT) every day in Oct 2018, Jan 2019, Apr 2019 and July 2019
Number of backward running days	3
Number of releasing particles	20 000
OH reaction	On and off
Meteorological data	NCEP CFSv2 with $0.5° \times 0.5°$ horizontal resolution and 64 vertical levels (Saha et al., 2014)
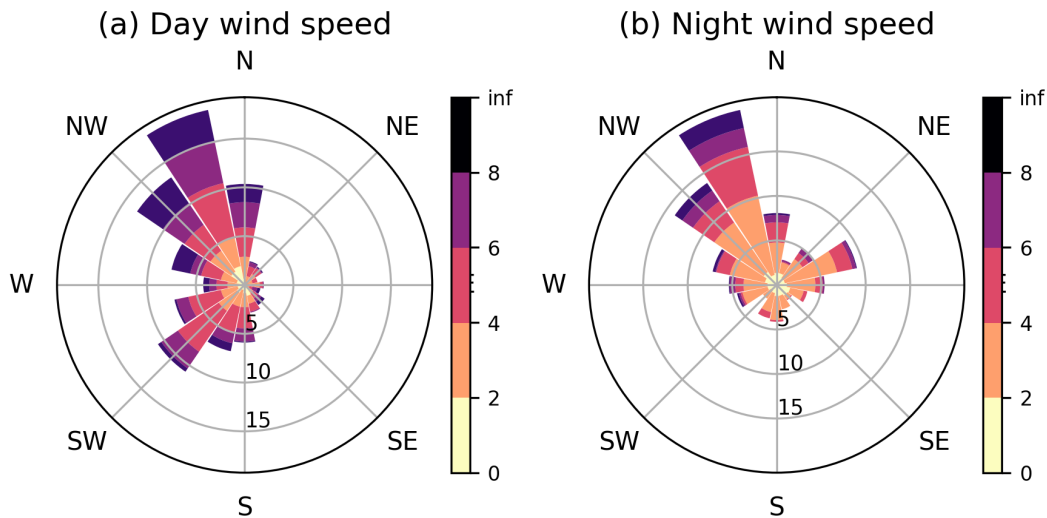
Figure C1. Wind rose from WRF-GHG simulations during the afternoon (13h - 18h LT) (a) and at night (3h - 8h LT) (b). The colors indicate the associated wind speed (in m s^{-1}), while the lengths of the bars show the frequency of any wind direction binned by 22.5 °, given in percentage.

Acknowledgements. We would like to thank all staff at the Xianghe site for operating the FTIR and PICARRO measurements. This work is supported by the National Natural Science Foundation of China (No. 42205140; 41975035). Emmanuel Mahieu is a senior research associate with the F.R.S.-FNRS. The authors acknowledge all providers of observational data and emission inventories. We thank the IT team at BIRA-IASB for their support on data storage and HPC maintenance. Christophe Gerbig, Roberto Kretschmer, and Thomas Koch (MPI BGC) are thanked for distributing the VPRM preprocessor code. Finally, we are grateful for fruitful discussions with Jean-François Müller (BIRA-IASB) and Bernard Heinesch (ULiège).

595

References

TROPOMI Level 2 Methane Total Column Products. Version 02, https://doi.org/10.5270/S5P-3lcdqiv, 2021.

Agustí-Panareda, A., Barré, J., Massart, S., Inness, A., Aben, I., Ades, M., Baier, B. C., Balsamo, G., Borsdorff, T., Bousserez, N., Boussetta, S., Buchwitz, M., Cantarello, L., Crevoisier, C., Engelen, R., Eskes, H., Flemming, J., Garrigues, S., Hasekamp, O., Huijnen, V., Jones, L., Kipling, Z., Langerock, B., McNorton, J., Meilhac, N., Noël, S., Parrington, M., Peuch, V.-H., Ramonet, M., Razinger, M., Reuter, M., Ribas, R., Suttie, M., Sweeney, C., Tarniewicz, J., and Wu, L.: Technical Note: The CAMS Greenhouse Gas Reanalysis from 2003 to 2020, Atmospheric Chemistry and Physics, 23, 3829–3859, https://doi.org/10.5194/acp-23-3829-2023, 2023.

Ahmadov, R., Gerbig, C., Kretschmer, R., Koerner, S., Neininger, B., Dolman, A. J., and Sarrat, C.: Mesoscale Covariance of Transport and CO2 Fluxes: Evidence from Observations and Simulations Using the WRF-VPRM Coupled Atmosphere-Biosphere Model, Journal of Geophysical Research: Atmospheres, 112, https://doi.org/10.1029/2007JD008552, 2007.

Apituley, A., Pedergnana, M., Sneep, M., Veefkind, P. J., Loyola, D., Hasekamp, O., Lorente Delgado, A., and Borsdorff, T.: Sentinel-5 precursor/TROPOMI Level 2 Product User Manual Methane, Tech. rep., SRON/KNMI, ref: SRON-S5P-LEV2-MA-001, issue: 2.6.0, 2023.

Asefi-Najafabady, S., Rayner, P. J., Gurney, K. R., McRobert, A., Song, Y., Coltin, K., Huang, J., Elvidge, C., and Baugh, K.: A Multiyear, Global Gridded Fossil Fuel CO_2 Emission Data Product: Evaluation and Analysis of Results: GLOBAL FOSSIL FUEL CO2 EMISSIONS, Journal of Geophysical Research: Atmospheres, 119, 10,213–10,231, https://doi.org/10.1002/2013JD021296, 2014.

Beck, V., Koch, T., Kretschmer, R., Marshall, J., Ahmadov, R., Gerbig, C., Pillai, D., and Heimann, M.: The WRF Greenhouse Gas Model (WRF-GHG), 2011.

Bloom, A., Bowman, K., Lee, M., Turner, A., Schroeder, R., Worden, J., Weidner, R., McDonal, K., and Jacob, D.: CMS: Global 0.5-Deg Wetland Methane Emissions and Uncertainty (WetCHARTs v1.0), https://doi.org/10.3334/ORNLDAAC/1502, 2017.

Callewaert, S.: WRF-Chem Simulations of CO2, CH4 and CO around Xianghe, China, https://doi.org/10.18758/P34WJEW2, 2023.

Callewaert, S., Brioude, J., Langerock, B., Duflot, V., Fonteyn, D., Müller, J.-F. c., Metzger, J.-M., Hermans, C., Kumps, N., Ramonet, M., Lopez, M., Mahieu, E., and De Mazière, M.: Analysis of CO_2, CH_4, and CO Surface and Column Concentrations Observed at Réunion Island by Assessing WRF-Chem Simulations, Atmospheric Chemistry and Physics, 22, 7763–7792, https://doi.org/10.5194/acp-22-7763-2022, 2022.

Chen, Z., Jacob, D. J., Nesser, H., Sulprizio, M. P., Lorente, A., Varon, D. J., Lu, X., Shen, L., Qu, Z., Penn, E., and Yu, X.: Methane Emissions from China: A High-Resolution Inversion of TROPOMI Satellite Observations, Atmospheric Chemistry and Physics, 22, 10 809–10 826, https://doi.org/10.5194/acp-22-10809-2022, 2022.

Crippa, M., Guizzardi, D., Muntean, M., and Schaaf, E.: EDGAR v5.0 Global Air Pollutant Emissions., http://data.europa.eu/89h/377801af-b094-4943-8fdc-f79a7c0c2d19, 2019.

Crippa, M., Solazzo, E., Huang, G., Guizzardi, D., Koffi, E., Muntean, M., Schieberle, C., Friedrich, R., and Janssens-Maenhout, G.: High Resolution Temporal Profiles in the Emissions Database for Global Atmospheric Research, Scientific Data, 7, 121, https://doi.org/10.1038/s41597-020-0462-2, 2020.

Dayalu, A., Munger, J. W., Wofsy, S. C., Wang, Y., Nehrkorn, T., Zhao, Y., McElroy, M. B., Nielsen, C. P., and Luus, K.: Assessing Biotic Contributions to CO_2 Fluxes in Northern China Using the Vegetation, Photosynthesis and Respiration Model (VPRM-CHINA) and Observations from 2005 to 2009, Biogeosciences, 15, 6713–6729, https://doi.org/10.5194/bg-15-6713-2018, 2018.

Dekker, I. N., Houweling, S., Aben, I., Röckmann, T., Krol, M., Martínez-Alonso, S., Deeter, M. N., and Worden, H. M.: Quantification of CO Emissions from the City of Madrid Using MOPITT Satellite Retrievals and WRF Simulations, Atmospheric Chemistry and Physics, 17, 14 675–14 694, https://doi.org/10.5194/acp-17-14675-2017, 2017.

Dong, X., Yue, M., Jiang, Y., Hu, X.-M., Ma, Q., Pu, J., and Zhou, G.: Analysis of CO_2 Spatio-Temporal Variations in China Using a Weather–Biosphere Online Coupled Model, Atmospheric Chemistry and Physics, 21, 7217–7233, https://doi.org/10.5194/acp-21-7217-2021, 2021.

Dudhia, J.: Numerical Study of Convection Observed during the Winter Monsoon Experiment Using a Mesoscale Two-Dimensional Model, Journal of the Atmospheric Sciences, 46, 3077–3107, https://doi.org/10.1175/1520-0469(1989)046<3077:NSOCOD>2.0.CO;2, 1989.

Fast, J. D., Gustafson Jr., W. I., Easter, R. C., Zaveri, R. A., Barnard, J. C., Chapman, E. G., Grell, G. A., and Peckham, S. E.: Evolution of Ozone, Particulates, and Aerosol Direct Radiative Forcing in the Vicinity of Houston Using a Fully Coupled Meteorology-Chemistry-Aerosol Model, Journal of Geophysical Research: Atmospheres, 111, https://doi.org/10.1029/2005JD006721, 2006.

Feng, S., Lauvaux, T., Newman, S., Rao, P., Ahmadov, R., Deng, A., Díaz-Isaac, L. I., Duren, R. M., Fischer, M. L., Gerbig, C., Gurney, K. R., Huang, J., Jeong, S., Li, Z., Miller, C. E., O'Keeffe, D., Patarasuk, R., Sander, S. P., Song, Y., Wong, K. W., and Yung, Y. L.: Los Angeles Megacity: A High-Resolution Land–Atmosphere Modelling System for Urban CO_2 Emissions, Atmospheric Chemistry and Physics, 16, 9019–9045, https://doi.org/10.5194/acp-16-9019-2016, 2016.

Ferrario, F. M., Crippa, M., Guizzardi, D., Muntean, M., Schaaf, E., Vullo, E. L., Solazzo, E., Olivier, J., and Vignati, E.: EDGAR v6.0 Greenhouse Gas Emissions, http://data.europa.eu/89h/97a67d67-c62e-4826-b873-9d972c4f670b, 2021.

Friedlingstein, P., O'Sullivan, M., Jones, M. W., Andrew, R. M., Gregor, L., Hauck, J., Le Quéré, C., Luijkx, I. T., Olsen, A., Peters, G. P., Peters, W., Pongratz, J., Schwingshackl, C., Sitch, S., Canadell, J. G., Ciais, P., Jackson, R. B., Alin, S. R., Alkama, R., Arneth, A., Arora, V. K., Bates, N. R., Becker, M., Bellouin, N., Bittig, H. C., Bopp, L., Chevallier, F., Chini, L. P., Cronin, M., Evans, W., Falk, S., Feely, R. A., Gasser, T., Gehlen, M., Gkritzalis, T., Gloege, L., Grassi, G., Gruber, N., Gürses, O., Harris, I., Hefner, M., Houghton, R. A., Hurtt, G. C., Iida, Y., Ilyina, T., Jain, A. K., Jersild, A., Kadono, K., Kato, E., Kennedy, D., Klein Goldewijk, K., Knauer, J., Korsbakken, J. I., Landschützer, P., Lefèvre, N., Lindsay, K., Liu, J., Liu, Z., Marland, G., Mayot, N., McGrath, M. J., Metzl, N., Monacci, N. M., Munro, D. R., Nakaoka, S.-I., Niwa, Y., O'Brien, K., Ono, T., Palmer, P. I., Pan, N., Pierrot, D., Pocock, K., Poulter, B., Resplandy, L., Robertson, E., Rödenbeck, C., Rodriguez, C., Rosan, T. M., Schwinger, J., Séférian, R., Shutler, J. D., Skjelvan, I., Steinhoff, T., Sun, Q., Sutton, A. J., Sweeney, C., Takao, S., Tanhua, T., Tans, P. P., Tian, X., Tian, H., Tilbrook, B., Tsujino, H., Tubiello, F., van der Werf, G. R., Walker, A. P., Wanninkhof, R., Whitehead, C., Willstrand Wranne, A., Wright, R., Yuan, W., Yue, C., Yue, X., Zaehle, S., Zeng, J., and Zheng, B.: Global Carbon Budget 2022, Earth System Science Data, 14, 4811–4900, https://doi.org/10.5194/essd-14-4811-2022, 2022.

Fu, G. Q., Xu, W. Y., Yang, R. F., Li, J. B., and Zhao, C. S.: The Distribution and Trends of Fog and Haze in the North China Plain over the Past 30 Years, Atmospheric Chemistry and Physics, 14, 11 949–11 958, https://doi.org/10.5194/acp-14-11949-2014, 2014.

Gbode, I. E., Dudhia, J., Ogunjobi, K. O., and Ajayi, V. O.: Sensitivity of Different Physics Schemes in the WRF Model during a West African Monsoon Regime, Theoretical and Applied Climatology, 136, 733–751, https://doi.org/10.1007/s00704-018-2538-x, 2019.

Granier, C., Darras, S., Denier van der Gon, H., Doubalova, J., Elguindi, N., Galle, B., Gauss, M., Guevara, M., Jalkanen, J.-P., Kuenen, J., Liousse, C., Quack, B., Simpson, D., and Sindelarova, K.: The Copernicus Atmosphere Monitoring Service Global and Regional Emissions (April 2019 Version), https://doi.org/10.24380/D0BN-KX16, 2019.

Grell, G. A., Peckham, S. E., Schmitz, R., McKeen, S. A., Frost, G., Skamarock, W. C., and Eder, B.: Fully Coupled "Online" Chemistry within the WRF Model, Atmospheric Environment, 39, 6957–6975, https://doi.org/10.1016/j.atmosenv.2005.04.027, 2005.

Guevara, M., Jorba, O., Tena, C., Denier van der Gon, H., Kuenen, J., Elguindi, N., Darras, S., Granier, C., and Pérez García-Pando, C.: Copernicus Atmosphere Monitoring Service TEMPOral Profiles (CAMS-TEMPO): Global and European Emission Temporal Profile Maps for Atmospheric Chemistry Modelling, Earth System Science Data, 13, 367–404, https://doi.org/10.5194/essd-13-367-2021, 2021.

Hersbach, H., Bell, B., Berrisford, P., Biavati, G., Horányi, A., Munoz Sabater, J., Nicolas, J., Peubey, C., Radu, R., Rozum, I., Schepers, D., Simmons, A., Soci, C., Dee, D., and Thépaut, J.-N.: ERA5 Hourly Data on Pressure Levels from 1940 to Present., https://doi.org/10.24381/cds.bd0915c6, 2023a.

Hersbach, H., Bell, B., Berrisford, P., Biavati, G., Horányi, A., Munoz Sabater, J., Nicolas, J., Peubey, C., Radu, R., Rozum, I., Schepers, D., Simmons, A., Soci, C., Dee, D., and Thépaut, J.-N.: ERA5 Hourly Data on Single Levels from 1940 to Present., https://doi.org/10.24381/cds.adbb2d47, 2023b.

Hong, S.-Y., Noh, Y., and Dudhia, J.: A New Vertical Diffusion Package with an Explicit Treatment of Entrainment Processes, Monthly Weather Review, 134, 2318–2341, https://doi.org/10.1175/MWR3199.1, 2006.

Hu, C., Zhang, J., Qi, B., Du, R., Xu, X., Xiong, H., Liu, H., Ai, X., Peng, Y., and Xiao, W.: Global Warming Will Largely Increase Waste Treatment CH_4 Emissions in Chinese Megacities: Insight from the First City-Scale CH_4 Concentration Observation Network in Hangzhou, China, Atmospheric Chemistry and Physics, 23, 4501–4520, https://doi.org/10.5194/acp-23-4501-2023, 2023.

Hu, X.-M., Crowell, S., Wang, Q., Zhang, Y., Davis, K. J., Xue, M., Xiao, X., Moore, B., Wu, X., Choi, Y., and DiGangi, J. P.: Dynamical Downscaling of CO2 in 2016 Over the Contiguous United States Using WRF-VPRM, a Weather-Biosphere-Online-Coupled Model, Journal of Advances in Modeling Earth Systems, 12, e2019MS001 875, https://doi.org/10.1029/2019MS001875, 2020.

Iacono, M. J., Delamere, J. S., Mlawer, E. J., Shephard, M. W., Clough, S. A., and Collins, W. D.: Radiative Forcing by Long-Lived Greenhouse Gases: Calculations with the AER Radiative Transfer Models, Journal of Geophysical Research: Atmospheres, 113, https://doi.org/10.1029/2008JD009944, 2008.

Inness, A., Ades, M., Agustí-Panareda, A., Barré, J., Benedictow, A., Blechschmidt, A.-M., Dominguez, J. J., Engelen, R., Eskes, H., Flemming, J., Huijnen, V., Jones, L., Kipling, Z., Massart, S., Parrington, M., Peuch, V.-H., Razinger, M., Remy, S., Schulz, M., and Suttie, M.: The CAMS Reanalysis of Atmospheric Composition, Atmospheric Chemistry and Physics, 19, 3515–3556, https://doi.org/10.5194/acp-19-3515-2019, 2019.

Janjić, Z. s. I.: The Step-Mountain Eta Coordinate Model: Further Developments of the Convection, Viscous Sublayer, and Turbulence Closure Schemes, Monthly Weather Review, 122, 927–945, https://doi.org/10.1175/1520-0493(1994)122<0927:TSMECM>2.0.CO;2, 1994.

Ji, D., Zhou, M., Wang, P., Yang, Y., Wang, T., Sun, X., Hermans, C., Yao, B., and Wang, G.: Deriving Temporal and Vertical Distributions of Methane in Xianghe Using Ground-based Fourier Transform Infrared and Gas-analyzer Measurements, Advances in Atmospheric Sciences, 37, 597–607, https://doi.org/10.1007/s00376-020-9233-4, 2020.

Jiménez, P. A., Dudhia, J., González-Rouco, J. F., Navarro, J., Montávez, J. P., and García-Bustamante, E.: A Revised Scheme for the WRF Surface Layer Formulation, Monthly Weather Review, 140, 898–918, https://doi.org/10.1175/MWR-D-11-00056.1, 2012.

Keppel-Aleks, G., Wennberg, P. O., and Schneider, T.: Sources of Variations in Total Column Carbon Dioxide, Atmospheric Chemistry and Physics, 11, 3581–3593, https://doi.org/10.5194/acp-11-3581-2011, 2011.

Kurokawa, J. and Ohara, T.: Long-Term Historical Trends in Air Pollutant Emissions in Asia: Regional Emission Inventory in ASia (REAS) Version 3, Atmospheric Chemistry and Physics, 20, 12 761–12 793, https://doi.org/10.5194/acp-20-12761-2020, 2020.

Landschützer, P., Gruber, N., and Bakker, D. C. E.: An Observation-Based Global Monthly Gridded Sea Surface pCO_2 Product from 1982 Onward and Its Monthly Climatology (NCEI Accession 0160558). NOAA National Centers for Environmental Information., https://doi.org/10.7289/v5z899n6, 2017.

Laughner, J. L., Roche, S., Kiel, M., Toon, G. C., Wunch, D., Baier, B. C., Biraud, S., Chen, H., Kivi, R., Laemmel, T., McKain, K., Quéhé, P.-Y., Rousogenous, C., Stephens, B. B., Walker, K., and Wennberg, P. O.: A New Algorithm to Generate a Priori Trace Gas Profiles for the GGG2020 Retrieval Algorithm, Atmospheric Measurement Techniques, 16, 1121–1146, https://doi.org/10.5194/amt-16-1121-2023, 2023.

715 Laughner, J. L., Toon, G. C., Mendonca, J., Petri, C., Roche, S., Wunch, D., Blavier, J.-F., Griffith, D. W. T., Heikkinen, P., Keeling, R. F., Kiel, M., Kivi, R., Roehl, C. M., Stephens, B. B., Baier, B. C., Chen, H., Choi, Y., Deutscher, N. M., DiGangi, J. P., Gross, J., Herkommer, B., Jeseck, P., Laemmel, T., Lan, X., McGee, E., McKain, K., Miller, J., Morino, I., Notholt, J., Ohyama, H., Pollard, D. F., Rettinger, M., Riris, H., Rousogenous, C., Sha, M. K., Shiomi, K., Strong, K., Sussmann, R., Té, Y., Velazco, V. A., Wofsy, S. C., Zhou, M., and Wennberg, P. O.: The Total Carbon Column Observing Network's GGG2020 data version, Earth System Science Data, 16, 2197–2260, 720 https://doi.org/10.5194/essd-16-2197-2024, publisher: Copernicus GmbH, 2024.

Li, J., Hao, X., Liao, H., Wang, Y., Cai, W., Li, K., Yue, X., Yang, Y., Chen, H., Mao, Y., Fu, Y., Chen, L., and Zhu, J.: Winter Particulate Pollution Severity in North China Driven by Atmospheric Teleconnections, Nature Geoscience, 15, 349–355, https://doi.org/10.1038/s41561-022-00933-2, 2022.

Li, X., Hu, X.-M., Cai, C., Jia, Q., Zhang, Y., Liu, J., Xue, M., Xu, J., Wen, R., and Crowell, S. M. R.: Terrestrial CO2 Fluxes, Concentrations, 725 Sources and Budget in Northeast China: Observational and Modeling Studies, Journal of Geophysical Research: Atmospheres, 125, e2019JD031 686, https://doi.org/10.1029/2019JD031686, 2020.

Liu, Y., Yue, T., Zhang, L., Zhao, N., Zhao, M., and Liu, Y.: Simulation and Analysis of XCO2 in North China Based on High Accuracy Surface Modeling, Environmental Science and Pollution Research International, 25, 27 378–27 392, https://doi.org/10.1007/s11356-018-2683-x, 2018.

730 Maasakkers, J. D., Jacob, D. J., Sulprizio, M. P., Turner, A. J., Weitz, M., Wirth, T., Hight, C., DeFigueiredo, M., Desai, M., Schmeltz, R., Hockstad, L., Bloom, A. A., Bowman, K. W., Jeong, S., and Fischer, M. L.: Gridded National Inventory of U.S. Methane Emissions, Environmental Science & Technology, 50, 13 123–13 133, https://doi.org/10.1021/acs.est.6b02878, 2016.

Mahadevan, P., Wofsy, S. C., Matross, D. M., Xiao, X., Dunn, A. L., Lin, J. C., Gerbig, C., Munger, J. W., Chow, V. Y., and Gottlieb, E. W.: A Satellite-Based Biosphere Parameterization for Net Ecosystem CO2 Exchange: Vegetation Photosynthesis and Respiration Model 735 (VPRM), Global Biogeochemical Cycles, 22, https://doi.org/10.1029/2006GB002735, 2008.

Masson-Delmotte, V., Zhai, P., Pirani, A., Connors, S. L., Péan, C., Berger, S., Caud, N., Chen, Y., Goldfarb, L., Gomis, M. I., Huang, M., Leitzell, K., Lonnoy, E., Matthews, J. B. R., Maycock, T. K., Waterfield, T., Yelekçi, O., Yu, R., and Zhou (eds.), a. B.: IPCC, 2021: Climate Change 2021: The Physical Science Basis. Contribution of Working Group I to the Sixth Assessment Report of the Intergovernmental Panel on Climate Change, 2021.

740 Mlawer, E. J., Taubman, S. J., Brown, P. D., Iacono, M. J., and Clough, S. A.: Radiative Transfer for Inhomogeneous Atmospheres: RRTM, a Validated Correlated-k Model for the Longwave, Journal of Geophysical Research: Atmospheres, 102, 16 663–16 682, https://doi.org/10.1029/97JD00237, 1997.

Nakanishi, M. and Niino, H.: An Improved Mellor–Yamada Level-3 Model: Its Numerical Stability and Application to a Regional Prediction of Advection Fog, Boundary-Layer Meteorology, 119, 397–407, https://doi.org/10.1007/s10546-005-9030-8, 2006.

745 Nakanishi, M. and Niino, H.: Development of an Improved Turbulence Closure Model for the Atmospheric Boundary Layer, Journal of the Meteorological Society of Japan. Ser. II, 87, 895–912, https://doi.org/10.2151/jmsj.87.895, 2009.

Nassar, R., Napier-Linton, L., Gurney, K. R., Andres, R. J., Oda, T., Vogel, F. R., and Deng, F.: Improving the Temporal and Spatial Distribution of CO2 Emissions from Global Fossil Fuel Emission Data Sets, Journal of Geophysical Research: Atmospheres, 118, 917–933, https://doi.org/10.1029/2012JD018196, 2013.

750 Oda, T. and Maksyuto, S.: A Very High-Resolution (1 Km×1 Km) Global Fossil Fuel CO_2 Emission Inventory Derived Using a Point Source Database and Satellite Observations of Nighttime Lights, Atmospheric Chemistry and Physics, 11, 543–556, https://doi.org/10.5194/acp-11-543-2011, 2011.

Oda, T. and Maksyuto, S.: ODIAC Fossil Fuel CO_2 Emissions Dataset (ODIAC2020b), Center for Global Environmental Research, National Institute for Environmental Studies, https://doi.org/10.17595/20170411.001, 2020.

755 Oda, T., Maksyuto, S., and Andres, R. J.: The Open-source Data Inventory for Anthropogenic CO_2, Version 2016 (ODIAC2016): A Global Monthly Fossil Fuel CO_2 Gridded Emissions Data Product for Tracer Transport Simulations and Surface Flux Inversions, Earth System Science Data, 10, 87–107, https://doi.org/10.5194/essd-10-87-2018, 2018.

Olson, J. B., Kenyon, J. S., family=Angevine, given=Wayne. A., g.-i., Brown, J. M., Pagowski, M., and Suˇ selj, K.: A Description of the MYNN-EDMF Scheme and the Coupling to Other Components in WRF–ARW, https://doi.org/10.25923/n9wm-be49, 2019.

760 Park, C., Gerbig, C., Newman, S., Ahmadov, R., Feng, S., Gurney, K. R., Carmichael, G. R., Park, S.-Y., Lee, H.-W., Goulden, M., Stutz, J., Peischl, J., and Ryerson, T.: CO2 Transport, Variability, and Budget over the Southern California Air Basin Using the High-Resolution WRF-VPRM Model during the CalNex 2010 Campaign, Journal of Applied Meteorology and Climatology, 57, 1337–1352, https://doi.org/10.1175/JAMC-D-17-0358.1, 2018.

Park, C., Park, S.-Y., Gurney, K. R., Gerbig, C., DiGangi, J. P., Choi, Y., and Lee, H. W.: Numerical Simulation of Atmospheric CO2 Con-
765 centration and Flux over the Korean Peninsula Using WRF-VPRM Model during Korus-AQ 2016 Campaign, PLOS ONE, 15, e0228 106, https://doi.org/10.1371/journal.pone.0228106, 2020.

Parker, R. J., Wilson, C., Bloom, A. A., Comyn-Platt, E., Hayman, G., McNorton, J., Boesch, H., and Chipperfield, M. P.: Exploring Constraints on a Wetland Methane Emission Ensemble (WetCHARTs) Using GOSAT Observations, Biogeosciences, 17, 5669–5691, https://doi.org/10.5194/bg-17-5669-2020, 2020.

770 Pillai, D., Gerbig, C., Ahmadov, R., Rödenbeck, C., Kretschmer, R., Koch, T., Thompson, R., Neininger, B., and Lavrié, J. V.: High-resolution simulations of atmospheric CO₂ over complex terrain – representing the Ochsenkopf mountain tall tower, Atmospheric Chemistry and Physics, 11, 7445–7464, https://doi.org/10.5194/acp-11-7445-2011, 2011.

Pisso, I., Sollum, E., Grythe, H., Kristiansen, N. I., Cassiani, M., Eckhardt, S., Arnold, D., Morton, D., Thompson, R. L., Groot Zwaaftink, C. D., Evangeliou, N., Sodemann, H., Haimberger, L., Henne, S., Brunner, D., Burkhart, J. F., Fouilloux, A., Brioude, J., Philipp, A.,
775 Seibert, P., and Stohl, A.: The Lagrangian Particle Dispersion Model FLEXPART Version 10.4, Geoscientific Model Development, 12, 4955–4997, https://doi.org/10.5194/gmd-12-4955-2019, 2019.

Ramonet, M., Langerock, B., Warneke, T., and Eskes, H.: Validation Report of the CAMS Greenhouse Gas Global Reanalysis, Years 2003-2020, Tech. rep., KNMI, https://doi.org/10.24380/438C-4597, 2021.

Rodgers, C. D. and Connor, B. J.: Intercomparison of Remote Sounding Instruments, Journal of Geophysical Research: Atmospheres, 108,
780 n/a–n/a, https://doi.org/10.1029/2002JD002299, 2003.

Saha, S., Moorthi, S., Wu, X., Wang, J., Nadiga, S., Tripp, P., Behringer, D., Hou, Y.-T., Chuang, H.-y., Iredell, M., Ek, M., Meng, J., Yang, R., Mendez, M. P., van den Dool, H., Zhang, Q., Wang, W., Chen, M., and Becker, E.: The NCEP Climate Forecast System Version 2, https://doi.org/10.1175/JCLI-D-12-00823.1, 2014.

Saunois, M., Stavert, A. R., Poulter, B., Bousquet, P., Canadell, J. G., Jackson, R. B., Raymond, P. A., Dlugokencky, E. J., Houweling, S.,
Patra, P. K., Ciais, P., Arora, V. K., Bastviken, D., Bergamaschi, P., Blake, D. R., Brailsford, G., Bruhwiler, L., Carlson, K. M., Carrol,
M., Castaldi, S., Chandra, N., Crevoisier, C., Crill, P. M., Covey, K., Curry, C. L., Etiope, G., Frankenberg, C., Gedney, N., Hegglin,
M. I., Höglund-Isaksson, L., Hugelius, G., Ishizawa, M., Ito, A., Janssens-Maenhout, G., Jensen, K. M., Joos, F., Kleinen, T., Krummel,
P. B., Langenfelds, R. L., Laruelle, G. G., Liu, L., Machida, T., Maksyutov, S., McDonald, K. C., McNorton, J., Miller, P. A., Melton,
J. R., Morino, I., Müller, J., Murguia-Flores, F., Naik, V., Niwa, Y., Noce, S., O'Doherty, S., Parker, R. J., Peng, C., Peng, S., Peters, G. P.,
Prigent, C., Prinn, R., Ramonet, M., Regnier, P., Riley, W. J., Rosentreter, J. A., Segers, A., Simpson, I. J., Shi, H., Smith, S. J., Steele, L. P.,
Thornton, B. F., Tian, H., Tohjima, Y., Tubiello, F. N., Tsuruta, A., Viovy, N., Voulgarakis, A., Weber, T. S., van Weele, M., van der Werf,
G. R., Weiss, R. F., Worthy, D., Wunch, D., Yin, Y., Yoshida, Y., Zhang, W., Zhang, Z., Zhao, Y., Zheng, B., Zhu, Q., Zhu, Q., and Zhuang,
Q.: The Global Methane Budget 2000–2017, Earth System Science Data, 12, 1561–1623, https://doi.org/10.5194/essd-12-1561-2020,
2020.

Schulzweida, U.: Climate Data Operators (CDO) User Guide, 10.5281/zenodo.10020800, 2020.

Sha, M. K., Langerock, B., Blavier, J.-F. L., Blumenstock, T., Borsdorff, T., Buschmann, M., Dehn, A., De Mazière, M., Deutscher, N. M.,
Feist, D. G., García, O. E., Griffith, D. W. T., Grutter, M., Hannigan, J. W., Hase, F., Heikkinen, P., Hermans, C., Iraci, L. T., Jeseck,
P., Jones, N., Kivi, R., Kumps, N., Landgraf, J., Lorente, A., Mahieu, E., Makarova, M. V., Mellqvist, J., Metzger, J.-M., Morino, I.,
Nagahama, T., Notholt, J., Ohyama, H., Ortega, I., Palm, M., Petri, C., Pollard, D. F., Rettinger, M., Robinson, J., Roche, S., Roehl, C. M.,
Röhling, A. N., Rousogenous, C., Schneider, M., Shiomi, K., Smale, D., Stremme, W., Strong, K., Sussmann, R., Té, Y., Uchino, O.,
Velazco, V. A., Vigouroux, C., Vrekoussis, M., Wang, P., Warneke, T., Wizenberg, T., Wunch, D., Yamanouchi, S., Yang, Y., and Zhou,
M.: Validation of methane and carbon monoxide from Sentinel-5 Precursor using TCCON and NDACC-IRWG stations, Atmospheric
Measurement Techniques, 14, 6249–6304, https://doi.org/10.5194/amt-14-6249-2021, publisher: Copernicus GmbH, 2021.

Skamarock, C., Klemp, B., Dudhia, J., Gill, O., Liu, Z., Berner, J., Wang, W., Powers, G., Duda, G., Barker, D., and Huang, X.-
y.: A Description of the Advanced Research WRF Model Version 4.1, Tech. rep., National Center for Atmospheric Research,
https://doi.org/10.5065/1dfh-6p97, 2019.

Soulie, A., Granier, C., Darras, S., Zilbermann, N., Doumbia, T., Guevara, M., Jalkanen, J.-P., Keita, S., Liousse, C., Crippa, M., Guizzardi,
D., Hoesly, R., and Smith, S.: Global Anthropogenic Emissions (CAMS-GLOB-ANT) for the Copernicus Atmosphere Monitoring Service
Simulations of Air Quality Forecasts and Reanalyses, Earth System Science Data Discussions, pp. 1–45, https://doi.org/10.5194/essd-
2023-306, 2023.

Tian, Y., Hong, X., Shan, C., Sun, Y., Wang, W., Zhou, M., Wang, P., Lin, P., and Liu, C.: Investigating the Performance of Carbon Monoxide
and Methane Observations from Sentinel-5 Precursor in China, Remote Sensing, 14, 6045, https://doi.org/10.3390/rs14236045, 2022.

Wang, R., Tao, S., Ciais, P., Shen, H. Z., Huang, Y., Chen, H., Shen, G. F., Wang, B., Li, W., Zhang, Y. Y., Lu, Y., Zhu, D., Chen, Y. C.,
Liu, X. P., Wang, W. T., Wang, X. L., Liu, W. X., Li, B. G., and Piao, S. L.: High-Resolution Mapping of Combustion Processes and
Implications for CO_2 Emissions, Atmospheric Chemistry and Physics, 13, 5189–5203, https://doi.org/10.5194/acp-13-5189-2013, 2013.

Wiedinmyer, C., Akagi, S. K., Yokelson, R. J., Emmons, L. K., Al-Saadi, J. A., Orlando, J. J., and Soja, A. J.: The Fire INven-
tory from NCAR (FINN): A High Resolution Global Model to Estimate the Emissions from Open Burning, Geosci. Model Dev.,
https://doi.org/10.5194/gmd-4-625-2011, 2011.

Worden, J. R., Cusworth, D. H., Qu, Z., Yin, Y., Zhang, Y., Bloom, A. A., Ma, S., Byrne, B. K., Scarpelli, T., Maasakkers, J. D., Crisp,
D., Duren, R., and Jacob, D. J.: The 2019 Methane Budget and Uncertainties at 1° Resolution and Each Country through Bayesian

Integration Of GOSAT Total Column Methane Data and a Priori Inventory Estimates, Atmospheric Chemistry and Physics, 22, 6811–6841, https://doi.org/10.5194/acp-22-6811-2022, 2022.

Wunch, D., Toon, G. C., Blavier, J.-F. c. L., Washenfelder, R. A., Notholt, J., Connor, B. J., Griffith, D. W. T., Sherlock, V., and Wennberg, P. O.: The Total Carbon Column Observing Network, Philosophical Transactions of the Royal Society A: Mathematical, Physical and Engineering Sciences, 369, 2087–2112, https://doi.org/10.1098/rsta.2010.0240, 2011.

Yang, Y., Zhou, M., Langerock, B., Sha, M. K., Hermans, C., Wang, T., Ji, D., Vigouroux, C., Kumps, N., Wang, G., De Mazière, M., and Wang, P.: New Ground-Based Fourier-transform near-Infrared Solar Absorption Measurements of XCO_2, XCH_4 and XCO at Xianghe, China, Earth System Science Data, 12, 1679–1696, https://doi.org/10.5194/essd-12-1679-2020, 2020.

Yang, Y., Zhou, M., Wang, T., Yao, B., Han, P., Ji, D., Zhou, W., Sun, Y., Wang, G., and Wang, P.: Spatial and Temporal Variations of CO_2 Mole Fractions Observed at Beijing, Xianghe, and Xinglong in North China, Atmospheric Chemistry and Physics, 21, 11 741–11 757, https://doi.org/10.5194/acp-21-11741-2021, 2021.

Zhao, X., Marshall, J., Hachinger, S., Gerbig, C., Frey, M., Hase, F., and Chen, J.: Analysis of Total Column CO_2 and CH_4 Measurements in Berlin with WRF-GHG, Atmospheric Chemistry and Physics, 19, 11 279–11 302, https://doi.org/10.5194/acp-19-11279-2019, 2019.

Zhao, Y., Nielsen, C. P., and McElroy, M. B.: China's CO2 Emissions Estimated from the Bottom up: Recent Trends, Spatial Distributions, and Quantification of Uncertainties, Atmospheric Environment, 59, 214–223, https://doi.org/10.1016/j.atmosenv.2012.05.027, 2012.

Zhong, Q., Huang, Y., Shen, H., Chen, Y., Chen, H., Huang, T., Zeng, E. Y., and Tao, S.: Global Estimates of Carbon Monoxide Emissions from 1960 to 2013, Environmental Science and Pollution Research, 24, 864–873, https://doi.org/10.1007/s11356-016-7896-2, 2017.

Zhou, M., Wang, P., Kumps, N., Hermans, C., and Nan, W.: TCCON Data from Xianghe, China, Release GGG2020.R0 (Version R0), https://doi.org/10.14291/tccon.ggg2020.xianghe01.R0, 2022.